E-740

INVESTIGATION OF HEAVY QUARK PRODUCTION BY GLUON SPLITTING FROM ANALYSIS OF MUONS IN QCD JETS AT THE D-ZERO DETECTOR AT FERMI NATIONAL ACCELERATOR LABORATORY

A DISSERTATION SUBMITTED TO THE GRADUATE DIVISION OF THE UNIVERSITY OF HAWAII IN PARTIAL FULFILLMENT OF THE REQUIREMENTS FOR THE DEGREE OF

DOCTOR OF PHILOSOPHY

IN

PHYSICS

DECEMBER 1995

By

John M. Balderston

Dissertation Committee :

Michael W. Peters, Chairperson
David D. Bleecker
Thomas E. Browder
Pui K. Lam
Sandip S. Pakvasa

AAE2750

We certify that we have read this dissertation and that, in our opinion, it is satisfactory in scope and quality as a dissertation for the degree of Doctor of Philosophy in Physics.

DISSERTATION COMMITTEE

_____

Chairperson

_____

_____

_____

_____

To Serena and Natalie and all my family.

ACKNOWLEDGEMENTS

I owe many people a great deal of thanks and credit for helping me put this analysis and thesis together. Mostly I have to thank Prof. Michael W. Peters for his help, encouragement and support and for his decision to send me to Fermi National Accelerator Laborartory in the first place. He frequently helped me think through crucial aspects of my analysis and helped me focus on the right things.

Thanks to Mike Peters I was able to work with the finest people I have ever had the good fortune to work with. And to work at a pre-eminent research facility. I will always treasure the memory of this experience.

At D-Zero I was especially fortunate to have worked with and helped by Norm Graf, Jerry Blazey, Dan Green, Dave Hedin, Ken Johns, Dave Fein, Gene Alvarez and Chris Murphy. These guys gave me a lot of help and support and I'll always be grateful to them for their insighfulness and concerns.

Cary Yoshikawa helped me get situated and acclimated when I first arrived in April, 1991, and has been a constant friend and companion (compadre?). Our friendship was forged in the inferno of Tom Diehl's 'graduate student hell' - working on the muon chambers.

Special mention must be made of all the help, insight and guidance I received from Tom Browder who has been a generous friend and advisor.

I can't forget Mike Jones who patiently listened to my occasional inane ramblings and offered very constructive criticisms when they were needed.

And credit is of course due to the entire D-Zero collaboration.

ABSTRACT

The production of b and c quarks in QCD jets from $p\bar{p}$ collisions at $\sqrt{s}$=1.8 TeV is investigated using decays to muons and hadronic debris. The results are based on data collected at the DØ experiment during the 1992-1993 FermiLab collider run. Two jet events are investigated and the rate for $b\bar{b}$ and $c\bar{c}$ from gluon splitting is compared with analytic estimates based on perturbative QCD to $O(\alpha_s^3)$. Reasonable agreement is observed. The characteristics of gluon splitting to $b\bar{b}$ and $c\bar{c}$ followed by quark decay to a muon are interpreted statistically based on the HERWIG Monte Carlo.

Contents

ACKNOWLEDGEMENTS iv

ABSTRACT v

LIST OF TABLES ix

LIST OF FIGURES x

1 INTRODUCTION: THE NATURE OF MATTER 1

1.1 The Birth of Modern Physics 1

1.2 High Energy Physics 3

1.3 The Standard Model 4

1.4 The Big Bang 6

1.5 Goal of This Work 6

2 HEAVY QUARKS IN QCD JETS 9

2.1 Why Heavy Quark Physics? 9

2.2 Heavy Quark Production 10

2.2.1 Estimating Cross Sections 11

2.3 Estimates 14

2.4 Detection Techniques 15

2.4.1 Hadronizing Partons 15

2.4.2 Observing Heavy Quarks 17

3 COLLIDERS 20

3.1 Types of Accelerators 20

3.2 The Tevatron 20

3.2.1 Cockroft-Walton Pre-Accelerator 21

3.2.2 Linear Accelerator 22

3.2.3 Booster 22

3.2.4 Main Ring 22

3.2.5 $\bar{p}$ Storage Ring (Debuncher and Accumulator) 23

3.2.6 Tevatron 23

4 THE D-ZERO (DØ) DETECTOR 25

4.1 Introduction to the DØ Detector 25

4.2 DØ Calorimeter 26

4.2.1 Massless Gaps and The ICD 30

4.3 DØ Muon System 30

5 DATA SET 36

5.1 Trigger and Data Acquisition 36

5.1.1 The Level 0 Trigger 36

5.1.2 Level 1 and 1.5 Triggers 37

5.1.3 The Level 2 Trigger 37

5.1.4 Calorimeter Triggers 38

5.2 Offline Jet and Muon Reconstruction 38

5.2.1 Jet Reconstruction 38

5.2.2 Muon Reconstruction 42

5.3 Event Selection 44

6 ANALYSIS OF THE DATA SET 54

6.1 Approach 54

6.2 Monte Carlo 55

6.2.1 $\pi^{\pm}$ and $K^{\pm}$ Decay Estimates 55

6.2.2 Heavy Quark Estimates 58

6.2.3 Jet Widths 60

6.2.4 Event Topologies 63

6.2.5 Gluon Jet Population Estimate 65

6.2.6 Fits 65

7 CONCLUSION 81

REFERENCES 82

List of Tables

1 Quark Generations 8

2 Lepton Generations 8

3 Fundamental Forces 8

4 Central Calorimeter characteristics 29

5 Design parameters of the DØ muon system 35

6 Level 2 terms used in data selection 40

7 MC Estimates for Relative abundances of muons from different sources in jets 60

8 Estimated number of gluon jets by jet E_T bins 65

9 Unconstrained fit and Monte Carlo estimates for numbers of muons by source in total data set 68

10 Constrained fits for numbers of muons by source for the total data set 68

11 Constrained fits for numbers of muons by E_T^{jet} bins 68

12 Errors for rate for g$\rightarrow c\bar{c}$ 73

13 Errors for rate for g$\rightarrow b\bar{b}$ 73

14 Rates and errors by E_T^{jet} bin 74

List of Figures

1 Estimates for heavy quark production in gluon jets 16

2 LO ($O(\alpha_S^2)$) Feynman diagrams for quark production. 19

3 NLO ($O(\alpha_S^3)$) Feynman diagrams for quark production. 19

4 The Tevatron Collider at Fermilab. 21

5 Cutaway view of the DØ detector 26

6 The DØ calorimeter system. 27

7 Unit cell in the DØ calorimeter. 28

8 Elevation view of the DØ detector. 31

9 Total interaction lengths of calorimeter and muon system. 32

10 Equipotential lines of a muon PDT cell ; signal wire at +5 kV, vernier pads at +2 kV. 33

11 WAMUS PDT cathode pad structure. 34

12 B or C layer muon chamber 35

13 DØ Trigger and Data Acqusition System. 39

14 Level 1 Trigger processing stages 40

15 Characteristics of the data set 47

16 Jet E_T Balance of n-jet events selected 48

17 Lego plot of a typical Two Jet Event 49

18 End view of a typical Two Jet Event 50

19 Top view of a typical Two Jet Event 51

20 Lego plot of a typical Three Jet Event 52

21 End view of a typical Three Jet Event 53

22 HERWIG generated $\pi/K \rightarrow \mu$ distributions 59

23 HERWIG generated $b/c \rightarrow \mu$ distributions 61

24 HERWIG generated $b/c \rightarrow \mu$ distributions 62

25 MC particle level compared with data RMS η and ϕ widths 64

26 Distributions used to calculate the Number of Gluon Jets 66

27 Fit contour for $g \rightarrow c\bar{c}$ vs $g \rightarrow b\bar{b}$ 69

28 Projections for fit to total data set by sources 70

29 Projections of fit results compared to data in jet E_T bins 71

30 Rate for gluon splitting to $c\bar{c}$ 75

31 Fit for $g \rightarrow b\bar{b}$ and Estimate using $m_b = 4.25$ GeV/c^2 76

32 Fit for $g \rightarrow b\bar{b}$ and Estimate using $m_b = 4.5$ GeV/c^2 77

33 Fit for $g \rightarrow b\bar{b}$ and Estimate using $m_b = 4.75$ GeV/c^2 78

34 Fit for $g \rightarrow b\bar{b}$ and Estimate using $m_b = 5.0$ GeV/c^2 79

35 Fit for $g \rightarrow b\bar{b}$ and Estimate using $m_b = 5.25$GeV/c^2 80

1 INTRODUCTION : THE NATURE OF MATTER

People have always sought fundamental understanding of the world around them. Among the first descriptions of nature was one that asserted that everything was composed of parts of earth, air, fire and water. That description reflected the extent of the ability of the ancient Greeks to test and observe their surroundings. Later, with observations of smoke particles, came the notion that matter could be reduced to infinitesimal elements which Democritus called atoms.

1.1 The Birth of Modern Physics

Much later experimental ability advanced to the point where the world of atoms could be explored. The first investigations of the atom showed it had components with opposite electric charges. The negatively charged entities were called electrons. J. J. Thompson, observing the interactions of these components, formulated the 'Plum Pudding' model which had negatively charged electrons imbedded in a large positvely charged sphere. This model gave good agreement between the calculated frequencies of vibration modes of the electrons in the 'Pudding' and the observed spectral frequencies. His model was as good as his capability to test it.

As experimental capabilities improved, understanding of the atom improved. Rutherford showed in α-particle scattering experiments that atoms did not behave like pudding, rather they behaved more like largely empty bodies - electron charge separated from a small, hard, positively charged center or nucleus.

Early in the 19th century, Mendeleev observed that when the elements were arranged in order of mass, they fell into groups that spanned periods. This is the periodic table of elements. It wasn't until the 20th century that through Pauli's exclusion principle, born of experiment and advances in quantum theory, the periodic table was understood.

Up to 1932 the only known elementary particles were the photon, electron and proton. After the development of quantum mechanics and the discovery of the Dirac equation it appeared the photon and electron were understood. This led to the understanding of the elctron's magnetic moment, expressed as:

$$\mu_e = \frac{-e}{2m_e}\,\sigma$$

with σ the spin of the electron and assuming the natural units where $\hbar = c = 1$. It was expected that the proton would have a magnetic moment:

$$\mu_p = \frac{-e}{2m_p}\,\sigma$$

but this was found not to be the case. Experiments by O. Stern showed that the magnetic moment of the proton was substantially different from the expected value (about 2.5 times), indicating the proton had a structure of charged components. This revealed another force besides gravitation and electromagnetism. This was the strong force, followed a little later by the discovery by Fermi of the weak force in β decay.

Yukawa assumed the nuclear force binding the proton's constituents was described by a wave field satisfying the Klein-Gordon equation:

$$(\Box + m^2)U(x) = g\rho(x)$$

where $\rho(x)$ is a nucleon density function and g is a coupling constant. From the solution to this equation and dimensional arguments (the interaction takes place within the proton) the mass of the mediating particle was estimated at between 20 and 200 MeV. When the π meson was discovered in cosmic rays (Lattes 1947) and was found to have a mass of around 140 MeV, it was thought that this was the mediator of the strong force. The neutral π meson was discovered later (Carlson 1950; Bjorkland 1950) with about the same mass.

Because the proton and neutron are similar in mass, as are the neutral and charged pions, it was thought that these were different states in the same set of elementary particles and that they belonged to an invariance group. In analogy to spin this invariance group was called isospin, an abstract transformation group in the space of state vectors. The proton and neutron can be taken as basis vectors of a two dimnensional space and isospin rotation is an SU(2) transformation in this space. The same is true for the charged and neutral pions.

With relativistic quantum field theory, first proposed by Dirac, a description of the behaviour of particles was developed. This theory included particles interacting with fields and successfully described electromagnetic interactions between charged bodies mediated by spin 1 photons. Dirac brought this work to completion, which resulted in the theory called quantum electrodynamics (QED).

1.2 High Energy Physics

Investigating nuclear components requires resolving objects smaller than the nucleus. Because the detection of an object by reflection or refraction of waves is, limited by the wavelength used, detection of objects in the nucleus requires light

of wavelength shorter than the diameter of the nucleus. For example, if a typical atomic diameter is 1 angstrom or 10^{-10}m and the nucleus typically 1 fermi or 10^{-13}m, a photon would need a frequency corresponding to an energy of around 12 MeV just to 'see' the nucleus.

As higher energies for probing the nucleus became available, new phenomena were observed which revealed previously unseen patterns and symmetries. When a proton is bombarded by another particle or photon of sufficient energy, particles other than the proton are observed. These new particles are called hadrons. Other particles called leptons (electrons, muons and taus) are also observed.

1.3 The Standard Model

Tables 1 and 2 list the fundamental particles of nature and the fundamental forces are listed in table 3. Interactions between the fundamental particles are understood in terms of quantum field theories.

Quantum Electrodynamics describes Electromagnetic interactions mediated by spin 1 photons. Further theoretical development, verified by experiment, found that Weak interactions are another manifestation of this same field theory, renamed the Electro-Weak theory or the Glashow-Salam-Weinberg Model [1]. The electro-weak interaction is described in terms of the symmetry group $SU(2)_L \times U(1)_Y$ which requires $(2^2 - 1) + (1)^2 = 4$ gauge bosons. The gauge bosons would be massless except that to describe weak force phenomenology the mediators require non-zero mass. Spontaneous symmetry breaking via the Higgs Mechanism [2] introduces complex scalar fields which are allowed to acquire a non-zero expectation value. In this way 3 of the 4 gauge vector bosons acquire

mass. These three are the W^+ and W^- mediating charged current interactions, and the Z^0, mediating neutral current interactions. The remaining vector boson, A, is identified with the photon and mediates electromagnetic interactions.

Finally, the strong force causes interactions only between quarks. It is described in terms of the color group $SU(3)_C$ with $(3^2 - 1) = 8$ masslesymmetry of the color interaction is non-Abelian which allows the gluons to interact with each other as well as mediate the strong force between quarks. This gauge theory is called Quantum Chromodynamics or QCD [3].

Particles which interact via the strong interaction are collectively known as hadrons. They are either mesons composed of a quark-antiquark pair or baryons composed of three quarks. As free quarks have not been observed, it is accepted that only color singlet or color neutral states arise in nature. This implies the concept of color confinement which is essential for describing the propagation and development of QCD jets.

The standard model is a Lagrangian Quantum Field Theory based on local gauge invariance and built up from the electroweak and strong gauge invariances. The symmetry group of the Standard Model is thus $SU(3)_C \times SU(2)_L \times U(1)_Y$ and a particle will have a wavefunction described in terms of its properties:

$$\psi = \psi_{space}\psi_{spin}\psi_{flavor}\psi_{color}$$

Hadronic interactions are described by the QCD Lagrangian :

$$\mathcal{L}_{QCD} = -\frac{1}{4}F_a^{\mu\nu}F_{a\mu\nu} + \overline{\psi}_j(i\gamma_\mu D^\mu - M)\psi_j$$

with a referring to the gauge bosons (8 bi-colored gluons).

One remaining force, gravitation, is mediated by spin 2 gravitons, but operates with a much lower strength than the other fundamental forces.

1.4 The Big Bang

High Energy Physics investigates fundamentals of nature. We see how nature behaves by experimental observations, and theoretical predictions are tested by experiment. Observations of the relative strength of the fundamental forces as a function of energy scale suggest a Unification Scale. At this scale the fundamental forces would have the same strength. Cosmological theories indicate that the universe originated in a Big Bang. The two theories, though separate, are not incompatible.

The Big Bang requires larger energy scales than anything we see occurring in the universe today. A model describing the Big Bang is now being tested and there is already some evidence for its validity in the mutual recession of galaxies, in the uniform background radiation permeating the universe and in the relative abundances of light elements found in the universe (predicted by big bang nucleosynthesis).

In colliders we explore conditions approximating the Big Bang, conditions where energy condenses to quarks, bound by gluons, and leptons which subsequently decay into others quarks and leptons until stable particles are formed.

1.5 Goal of This Work

The goal of this work is to test the Standard Model description for the production of heavy quark pairs from gluon splitting. The interaction of colliding hadrons

(proton and anti-proton) results in production of partons with high transverse momentum. These partons include both gluons and quarks and while both can radiate gluons and emit secondary quark-anti-quark pairs, resulting in jets of particles roughly along the direction of the original parton, only the gluons are able to directly split into $q\overline{q}$ pairs.

In this analysis heavy quarks are detected by their semileptonic decays to muons in the jets. The characteristics of these muons and the jets they are associated with are used together with the HERWIG Monte Carlo model to determine the fraction of muons from heavy quarks (b and c) coming from gluon splitting.

Table 1: Quark Generations

Quarks				
symbol	name	charge	rest mass	
u	up	$+2/3$	$2-8$	$\mathrm{MeV/c^2}$
d	down	$-1/3$	$5-15$	$\mathrm{MeV/c^2}$
c	charm	$+2/3$	$1-1.6$	$\mathrm{GeV/c^2}$
s	strange	$-1/3$	$100-300$	$\mathrm{MeV/c^2}$
t	top	$+2/3$	>170	$\mathrm{GeV/c^2}$
b	bottom	$-1/3$	$4.1-4.5$	$\mathrm{GeV/c^2}$

Table 2: Lepton Generations

Leptons				
symbol	name	charge	rest mass	
e	electron	-1	511	$\mathrm{KeV/c^2}$
ν_e	neutrino	0	<5	$\mathrm{eV/c^2}$
μ	muon	-1	105.7	$\mathrm{MeV/c^2}$
ν_μ	mu-neutr.	0	<0.27	$\mathrm{MeV/c^2}$
τ	tau	-1	1.8	$\mathrm{GeV/c^2}$
ν_{tau}	tau-neutr.	0	<31	$\mathrm{MeV/c^2}$

Table 3: Fundamental Forces

Force	range	mediator	relative strength
gravitational	∞	graviton	10^{-40}
weak	10^{-16} cm	W^+, W^-, Z^0	10^{-6}
electromagnetic	∞	photon	10^{-2}
strong	10^{-13} cm	gluon	1

2 HEAVY QUARKS IN QCD JETS

2.1 Why Heavy Quark Physics?

As physicists attempted to explain particle interactions in terms of light quarks u, d and s, and left-handed doublets of leptons $(\nu_e e^-)_L$ and $(\nu_\mu \mu^-)_L$, it seemed there should be another quark complementing the s as u complemented d in charge. The existence of charm was postulated to support two quark doublets $(ud_c)_L$ and $(cs_c)_L$ in analogy with the lepton doublets. The subscript c refers to mixtures of s and d quarks rotated by the Cabibbo angle.. In addition, Glashow, Iliopoulis and Maiani suggested the introduction of the c quark as a means for supressing strangeness-changing neutral currents, the GIM mechanism [5]. The existence of the charm quark was first conclusively demonstrated with the observation of the J/ψ, a $c\bar{c}$ state, in November 1974 at a resonance mass of 3.097 GeV / c^2 [6]. In 1977 evidence for the existence of a fifth quark dubbed *beauty* or *bottom*, was obtained in experiments at Fermilab [7]. The c and b quarks are the heavy quarks referred to in this work. Heavy quark physics provides an opportunity to investigate some interesting aspects of the standard model. Particularly interesting are the phenomenology of CP (charge-parity) violation and of mixing. These were first observed in the neutral K meson system, made from strange (s) quarks, where the particle (K^0) is observed to mix with its anti-particle ($\overline{K}^0$). Decay modes for the eigenstates of the $K^0/\overline{K}^0$ system, denoted K_L and K_S, are different under invariance of the combined unitary operators C (charge conjugation) and P (parity). Observation of decay modes common to both indicated violation of the principle of CP invariance. In the neutral B meson system ($B^0/\overline{B}^0$), with b quarks, the effect is more dramatic as the b mass is much larger than the s mass.

2.2 Heavy Quark Production

It has been known for some time that at hadron colliders the cross section for heavy quark production is high ($O(30\mu b)$) [8] in comparison to the cross section at electron-positron colliders ($O(nb)$). Although the signals from heavy quarks are invariably buried in a background of other processes, b production at hadron colliders has been conclusively observed by UA1, CDF and DØ [9] using high P^T leptons.

Theoretical calculations according to the Standard Model are relatively straightforward with some simplifications. There are several basic mechanisms which can be described in terms of perturbative expansions. Calculating individual terms can be very complex because radiative corrections and self-couplings result in infinities. These are addressed by renormalization techniques that enable these expansions to be evaluated. Ultra-violet singularities result without these renormalizations.

Fig. 2 shows examples of heavy quark production mechanisms in lowest order of the coupling constant ($O(\alpha_s^2)$) and without loop corrections. These are called direct production mechanisms. In observations of charm production in jets at the UA1 detector [10], it was found that calculations of $O(\alpha_s^2)$ could not account for the production observed rate. Later it was determined that the next higher order, of which examples are shown in Fig. 3, was more significant. In particular, the mechanism where a gluon fragments into a $q\overline{q}$ pair cannot be neglected.

2.2.1 Estimating Cross Sections

For hadron-hadron collisions resulting in two high P_T jets, the lowest order ($O(\alpha_s^2)$) calculation involves two-body to two-body processes (see Fig. 2). Perturbative QCD suggests a standardized form for the calculation [11]:

$$d\sigma_{H_1H_2} = \sum_{i,j} \int_0^1 dx_1 \int_0^1 dx_2 d\hat{\sigma}_{ij}(x_1P_1, x_2P_2, k_1, k_2, m, \mu) f_i^{H_1}(x_1, \mu) f_j^{H_2}(x_2, \mu)$$

with $k_{1,2}$ the momenta of the outgoing partons, $f_i^{H_1}$ the structure function for the ith parton in hadron H_1 and similarly for j in H_2. P_1 and P_2 are the momenta of hadrons 1 and 2 and $d\hat{\sigma}_{ij}$ is the elastic cross section for parton i scattering off of parton j. The parton mass is m and μ is the subtraction scale for ultraviolet and collinear divergences.

Perturbative QCD gives the prescription for calculating $d\hat{\sigma}_{ij}$ as a power series expansion in $\alpha_s(m^2)$. The quantity α_s represents the effective coupling between colored objects, which, because of vacuum polarization, depends on the momentum transfer between the objects.

In Quantum Electrodynamics (QED), measuring an electric charge at momentum transfer Q^2 with respect to a reference momentum transfer Q_0^2 shows effective screening from virtual electron/positron pairs. This modifies the electric charge 'seen' by the probe according to:

$$\alpha(Q^2) = \frac{\alpha(Q_0^2)}{1 - \frac{\alpha(Q_0^2)}{3\pi} log \frac{Q^2}{Q_0^2}}$$

This form is obtained by summing the expansion terms that go like $\alpha^n(log(\frac{Q^2}{Q_0^2}))^m$, keeping only the leading log ($m = n$) terms. This is referred to as the leading log approximation.

In QCD the color charge is screened and the same form would be expected if it were not for the mediators (gluons) which also carry color charge (unlike the photons in QED). In this case, polarization of gluon pairs in loops can have an anti-screening effect which increases the coupling or strength. Therefore, there are potential divergences in the perturbative QCD expansion.

To address UV divergence a renormalization scheme was developed. A (completely arbitrary) momentum scale μ_r with the dimension of mass is chosen. The rules for assigning the value of this parameter are renormalization schemes. In the Momentum Subtraction scheme, μ_r is chosen so that the mass of the propagator is zero at a fixed set of momenta. The value of μ_r varies according to the diverging loop integrals.

In the minimal subtraction scheme ($\overline{MS}$) μ_r is chosen to be the same for all divergent loop integrals and appears as a free parameter in the renormalized cross-sections.

After considering vacuum polarization, renormalizing and summing the leading log terms of the expansion, the QCD running coupling constant is given by

$$\alpha_s(Q^2) = \frac{\alpha_s(\mu_r^2)}{1 + \frac{\alpha_s(\mu_r^2)}{12\pi}(11N_c - 2n_f)log(Q^2/\mu_r^2)}$$

where N_c is the number of colors, n_f is the number of light flavors and Q^2 is the energy scale. For low Q^2, this coupling constant can become large at a scale denoted by:

$$\Lambda_{QCD}^2 = \mu_r^2 exp\frac{12\pi}{(11N_c - 2n_f)\alpha_s(\mu_r^2)}$$

The running coupling constant can then be re-expressed as:

$$\alpha_s(Q^2) = \frac{12\pi}{(11N_c - 2n_f)log(Q^2/\Lambda_{QCD}^2)}$$

Thus Λ^2_{QCD} determines the range of momentum transfer where perturbative QCD gives reliable results.

As aids for calculating terms in the total contribution to the cross section, Feynman diagrams are used. Leading order Feynman tree diagrams (ie. without renormalization loops) resulting in two final state partons are shown in Fig. 2 and examples of tree diagrams for the next higher order are shown in Fig. 3. There are two mechanisms resulting in production of heavy quark pairs: the so-called flavor creation mechanism, where the outgoing partons are the heavy quark pair, and gluon fragmentation where an outgoing gluon fragments into a heavy quark pair. In the first case the phenomenon occurs at high momentum transfer and so can be calculated perturbatively with little concern for non-perturbative correction. The second case is also calculated perturbatively and, even though it is to higher order in α_s, it appears this is the dominant production mechanism for heavy quark pairs in high P_T interactions. This is apparently the reason why experimental results, first reported by UA1 [12][13], indicated an excess in production of charmed mesons in jets.

We expect the contribution from gluon splitting will be larger than that from flavor creation or direct production of heavy quarks at Tevatron energies [14] because the inclusive cross-section for gluon jets is estimated to be about two orders of magnitude larger than the cross-section for direct quark production. Using the methods of perturbative QCD incorporating leading log terms, Mangano, Nason and Ridolfi[11] calculated cross sections for c and b quark production. Analyses by CDF and DØ [15] [16] have been compared with their estimates. The results are that CDF observed rates for $b\bar{b}$ production slightly in excess of the predic-

tion, while the DØ analysis yielded results within theoretical uncertainty of the prediction.

Thus the higher order terms are more significant than the leading order terms.

2.3 Estimates

In estimating the cross-section for heavy quarks, a convenient scale for μ_r is suggested by the quark mass. For the b quark this turns out to be appropriate at the energy scales currently being explored at the Tevatron. With the c quark , terms prpoportional to P_T/m_c begin to get larger and the scale is somewhat less clearly defined.

An estimate for the rate of high P_T gluon splitting into heavy quark pairs is made according to the calculation outlined by Mangano & Nason [24]:

$$rate = \frac{1}{6\pi}\int_{4m^2}^{Q^2}\frac{dK^2}{K^2}\alpha_s(K^2)(1+\frac{2m^2}{K^2})\sqrt{1-\frac{4m^2}{K^2}} \times n_g(Q^2,K^2)$$

Here, $n_g(Q^2,K^2)$ is the number of gluons with energy K^2 in a gluon with energy Q^2. The form Mangano and Nason derived for n_g, and the form used in calculating the curves shown in Fig. 1 is

$$n_g(Q^2,K^2) = \left(\frac{\log(Q^2/\Lambda^2)}{\log(K^2/\Lambda^2)}\right)^a \times \cosh\left(\sqrt{\frac{2C_A}{\pi b}}\left(\sqrt{\log\frac{Q^2}{\Lambda^2}} - \sqrt{\log\frac{K^2}{\Lambda^2}}\right)\right)$$

with b and a given by:

$$b = \frac{11C_A - 2N_F}{12\pi}$$

and

$$a = -\frac{1}{4}\left[1 + \frac{2C_A}{3\pi b}\left(1 - \frac{C_F}{C_A}\right)\right]$$

Using these equations, which are derived using two-loop estimates, the rates for $b\bar{b}$ and $c\bar{c}$ production in gluon jets are derived in the $\overline{MS}$ scheme. The results are shown in Fig. 1 using several different values for Λ_{QCD}.

2.4 Detection Techniques

2.4.1 Hadronizing Partons

Separation of quarks increases the density of the color field between them. This is called asymptotic freedom. With sufficient separation, the field density increases to the point that production of $q\bar{q}$ pairs can take place. As quarks are separated in hard collision processes, the energy of the recoiling quarks becomes manifest in production of $q\bar{q}$ pairs in jets of particles more or less collimated in the direction of the original scattered quark. But we do not observe bare quarks. We observe hadrons. A heavy quark is said to fragment when it hadronizes. A phenomenological model for this fragmentation was proposed by Peterson et. al [17] in a fragmentation function which describes the distribution of fractional momentum of a given hadron containing a heavy quark in a jet :

$$D_Q^H(z) = \frac{N}{z[1-(1/z)-\epsilon_Q/(1-z)]^2}$$

This is subject to the constraint that:

$$\sum_H \int dz D_Q^H(z) = 1$$

where the sum is over all hadrons H containing heavy quarks Q in the jet. With gluons, however, self-coupling allows for the radiation of gluons in addition to the creation of quark-antiquark pairs. This increases the calculational complexity of modeling the cascade of gluons. After gluons in cascades split into heavy quarks,

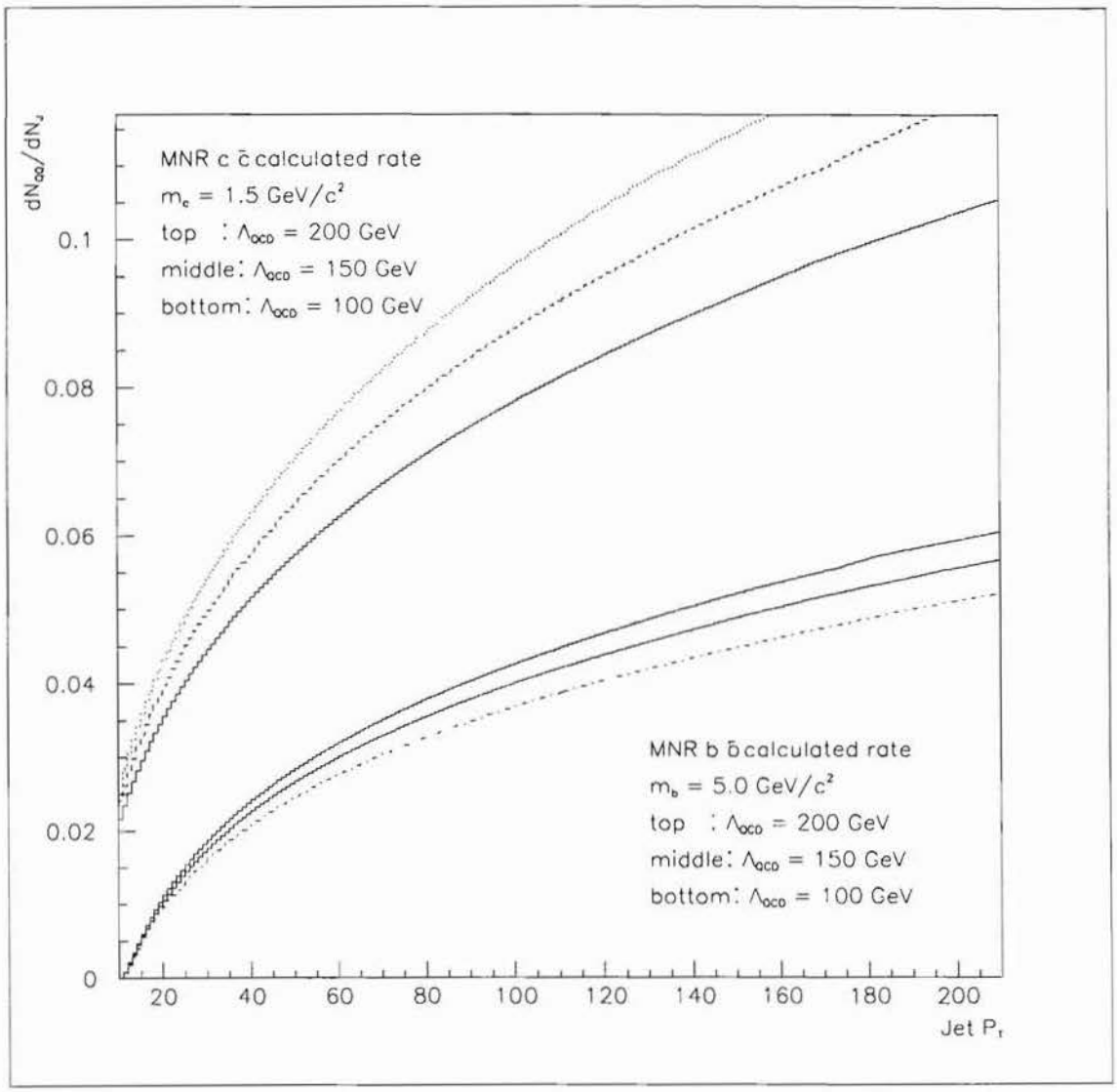

Figure 1: Estimates for heavy quark production in gluon jets

the quarks fragment into heavy hadrons. Signals from heavy hadrons indicate the presence of heavy quarks.

2.4.2 Observing Heavy Quarks

Because of asymptotic freedom, jets of hadrons form the direction of a parton scattered in a high energy interaction. The overall topology of the event indicates the underlying process of hard scattering. In events from $p\overline{p}$ collisions described by the diagrams of Fig. 2 we expect two outgoing jets with high transverse momenta relative to the $p\overline{p}$ axis. Next we look for evidence of the heavy quarks produced in these events. One method uses reconstructed tracks (in a magnetic field) of charged daughters of c hadrons ($D^{\pm}$) and b hadrons ($B^{\pm}$) and reconstructs the heavy meson that the daughters came from. The presence of the heavy quark is revealed by the presence of the heavy meson.

In this study heavy hadrons are detected by their weak decays to muons in jets. There are significant backgrounds to this signal from decays of $\pi^{+/-}$ and $K^{+/-}$ in flight and the characteristics and rates for these backgrounds are estimated by Monte Carlo techniques.

The decay of heavy mesons is described by the $V-A$ theory. The heavy hadron decays according to the spectator model, where the heavy quark is assumed to be at rest with respect to the partner, lighter quark. The decay is interpreted in terms of an off-shell or virtual W coupling between the quark and lepton pairs. The spectator model assumes that the momentum of the meson is the momentum of the heavy quark and so in the rest frame of the heavy meson the heavy quark is at rest with respect to the partner quark. The tag we use for bottom and charmed

hadrons and, consequently, for the b and c quarks in the jets, is the semileptonic decay muon from the heavy quark. Three-body kinematics indicate that the most likely transverse momentum of the muon from a heavy quark decay is half the Q value for the decay or the mass difference between the initial and final quark states. Thus for the Cabibbo-favored mode for $b \rightarrow c\mu\nu$, the most likely P_T^{rel} would be around 1.5 GeV/c^2 and for the $c \rightarrow s\mu\nu$ decay, around $0.3 - 0.8$ GeV/c^2. The quantity P_T^{rel} is defined to be :

$$P_T^{rel} = P_\mu \sin\theta$$

where the angle between the muon and the jet is θ.

A second characteristic variable is the momentum fraction of the muon along the jet axis, defined to be:

$$Z_{||} = \frac{\vec{p_\mu} \cdot \vec{p_{jet}}}{|\vec{p_{jet}}|^2}$$

The momentum fraction is expected to have a different shape depending on whether the jet is from a heavy quark or a gluon which split into heavy quarks.

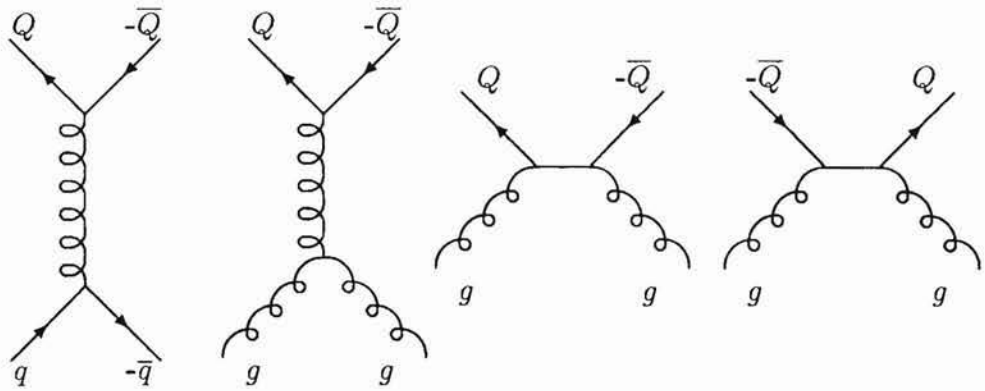

Figure 2: LO ($O(\alpha_S^2)$) Feynman diagrams for quark production.

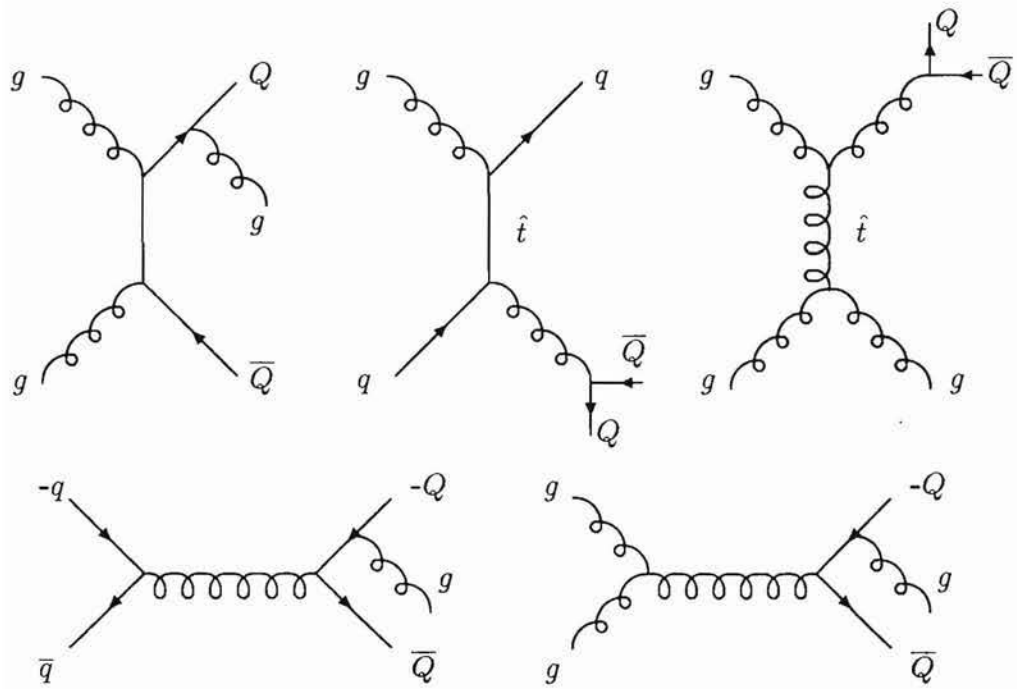

Figure 3: NLO ($O(\alpha_S^3)$) Feynman diagrams for quark production.

3 COLLIDERS

3.1 Types of Accelerators

Accelerators are machines for exploring matter at very small length scales, or at high energy. The two principle types are "fixed target" in which a beam of highly energetic particles is directed at a target at rest in the lab frame, and "colliders" which have two opposing beams of high energy particles interacting with each other. In terms of available energy, the colliding beam mode has a longer reach than the fixed target mode. The particles in the beams can be e^+/e^-, $p\bar{p}$ and ep - each has advantages and disadvantages. For instance, while $p\bar{p}$ colliders can achieve higher energies, they are susceptable to significant backgrounds from remnant particles while e^+/e^- colliders can produce cleaner events though at much lower energies.

The Tevatron at Fermilab can be run in both fixed target and collider modes. In collider mode, bunches of protons and antiprotons collide at 1.8 TeV.

3.2 The Tevatron

The Tevatron at Fermilab is currently the highest energy particle accelerator in the world. It produces collisions between proton and anti-protons beams at a $p\bar{p}$ center of momentum energy of 1.8 TeV [18]. Producing high energy collisions between proton and anti-proton beams is a multi-stage process of production and acceleration of the beams. This is accomplished through coordination of the following sub-systems :

1. Cockroft-Walton Pre-Accelerator.

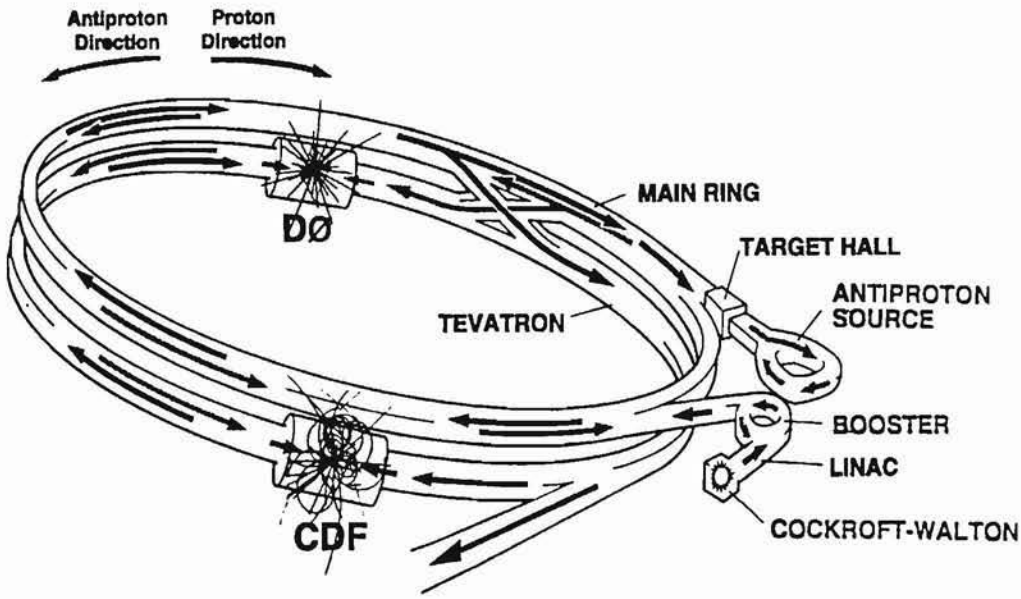

Figure 4: The Tevatron Collider at Fermilab.

2. The Linac (Linear Accelerator).
3. The Booster Synchrotron.
4. The Main Ring Accelerator.
5. The Pbar Storage Rings (Debuncher and Accumulator complex).
6. The Tevatron Ring.

See fig. 4 for the basic elements of the FermiLab Tevatron Collider Complex.

3.2.1 Cockroft-Walton Pre-Accelerator

In the pre-accelerator hydrogen molecules from a tank of H_2 gas are ionized to H^- and then the H^- ions are accelerated to an energy of 750 keV by a sequence of static electric fields.

3.2.2 Linear Accelerator

After leaving the Pre-Accelerator the beam of H^- ions is directed to the 150 m long Linac, a series of 9 RF (radio frequency) tanks. Here the ions are accelerated to 200 MeV. Quadrupole magnets are used for focusing the beam.

3.2.3 Booster

On exiting the Linac, the H^- ion beam passes through a carbon foil to remove all the electrons from the H^- ions. This leaves a beam of bare protons. The protons are then steered into the Booster Accelerator, a 151 m diameter synchrotron containing 18 RF cavities to accelerate the beam. Focusing and bending magnets keep the protons in a stable orbit and, as the beam momentum is increased, currents in the bending magnets are raised according to:

$$|\vec{p}| = \frac{qvB}{\rho}$$

In the booster protons are accelerated to 8 GeV. From here the beam is extracted and transferred to the Main Ring.

3.2.4 Main Ring

The Main Ring is a 2 km diameter synchrotron with over 1,000 copper-coil bending and focusing magnets used for proton beam confinement and stability. Dipole magnets are used to maintain the proton beam in a circular orbit while quadrupole magnets constrict the beam to a small cross-section. The Main Ring accelerates protons from 8 GeV to 150 GeV using RF electromagnetic fields.

3.2.5 $\bar{p}$ Storage Ring (Debuncher and Accumulator)

In producing $\bar{p}$'s, proton bunches from the Main Ring are extracted and directed at a nickel/copper target, producing approximately 20 million anti-protons from each proton bunch. The anti-protons are then injected into the $\bar{p}$ storage rings. When the $\bar{p}$'s first enter the ring, they have large variations in momentum. Many oscillate in directions transverse to the desired beam orbit. In a process known as stochastic cooling the transverse motions of the beam are reduced. The procedure involves sensors at one side of the ring detecting variations in $\bar{p}$ orbits. Correction signals are sent to kicker electrodes diametrically opposite the sensors while the deformed beam goes around the arc of the ring. This means that the correction signals will arrive at the kicker electrodes in time to correct the deformed beam. After cooling, the approximately 20 billion anti-protons are sent to the anti-proton Accumulator where further cooling takes place. Additional bunches added to the accumulator increase the density of stored $\bar{p}$'s. After 4 to 6 hours a store of about 200 billion anti-protons accumlates. This is enough for a 'shot' into the Tevatron.

3.2.6 Tevatron

After being accelerated to 150 GeV, proton and anti-proton bunches are injected into the Tevatron. Typically, the proton bunches contain around four to five times the number of particles as the anti-proton bunches, with the proton bunch size typically 6×10^{10} particles. In the Tevatron, particles are accelerated to 0.9 TeV. The Tevatron is housed in the Main Ring beam tunnel, about 60 cm below the Main Ring. Superconducting bending magnets cooled by liquid helium are used to produce the 2T magnetic fields to contain the high energy p and $\bar{p}$ beams. The

configuration used in this run was six bunches of protons and six bunches of anti-protons, counter-rotating in the Tevatron, brought to overlap at two interaction points around the ring. These are the sites designated B0 and D0. Collider detectors are installed in those locations. The Collider Detector at Fermilab (CDF) is situated at B0 and the D0 Detector at D0. Just outside these interaction points, special quadrupole magnets (called low-beta quadrupoles) are used to focus the beam to a cross-section of about 1 mm^2. During steady-state Tevatron operation, beam crossings happen every 3.5 μs. Due to scattering between beam bunches and residual gasses as well as beam-beam interactions, the density of the beams decreases with time. Beam lifetimes are typically 20 hours. Anti-proton accumulation remains continually active so a new 'stack' of anti-protons is usually available for subsequent shots. Stacking rates of 4.54×10^{10} $\bar{p}$/hour have been achieved. During the run in which the data for this analysis was taken, luminosities were typically about $5 \times 10^{30} cm^{-2} s^{-1}$, producing an average of about 1.2 interactions per crossing.

4 THE D-ZERO (DØ) DETECTOR

4.1 Introduction to the DØ Detector

The DØ detector [19] (Fig. 5) is a large, multi-purpose detector for studying $p\bar{p}$ interactions at $\sqrt{s} \cong 2$ TeV. The detector derives its name from its location in the Tevatron ring, that is, at the DØ beam crossing site. Its principle mission is to study high-mass states and high p_T phenomena. The principle areas of research are on the top quark, the bottom quark, W and Z physics, SUSY searches and perturbative QCD.

The DØ detector has thick magnetized iron absorbers for muon momentum measurement and suppression of hadronic punchthrough. It features good electron identification and momentum determination with a nearly hermetic and finely segmented calorimeter which is also well suited for measuring high P_T jets.

The detector rests on a support platform which can be rolled in and out of the DØ collision hall. Much of the front-end electronics for the detector subsystems are housed in the platform, with cables connecting the detector over an articulating bridge to the moveable counting house (MCH). The cable bridge and MCH are located outside the concrete shielding for the collision hall and are always accessible to researchers. Digitized information from the MCH is collected, zero suppressed and then passed on to data acquisition processor nodes located in the control room area.

Starting from the interaction point and moving outwards are the Central Detectors and Transition Radiation detectors, Calorimeter and Muon System. There was no central magnetic field during the run in which the data for this thesis was collected. The principal detectors used in this analysis were the Calorimeter and

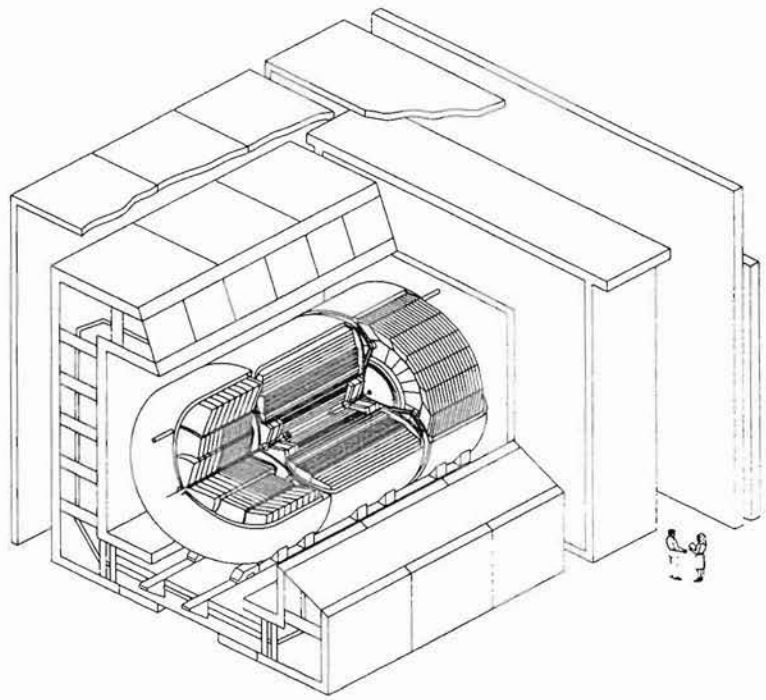

Figure 5: Cutaway view of the DØ detector

the Muon system.

4.2 DØ Calorimeter

The DØ detector uses a sampling calorimeter with depleted uranium, lead, copper and stainless steel as passive absorber and Liquid Argon as active absorber. There are three calorimeter systems (see fig 6): The Central, the North End and the South End Calorimeters.

The central calorimeter (CC) covers the pseudorapidity[1] range $|\eta| < 1.1$ while the end calorimeters (EC) cover the region $1.1 < |\eta| < 4.5$. In the gaps between the calorimeter systems, where the calorimeter absorber is not as thick because

[1] defined as $\eta = -\ln(\tan\frac{\theta}{2})$ where θ is the angle with respect to the beam axis.

of structural and support constraints, Inter Cryostat (IC) scintillator detectors and Massless Gaps (MG) scintillator detectors have been incorporated. As this analysis concerns central phenomena, discussion here is limited to the Central Calorimeter. The Central Calorimeter (CC) has three segments which are the

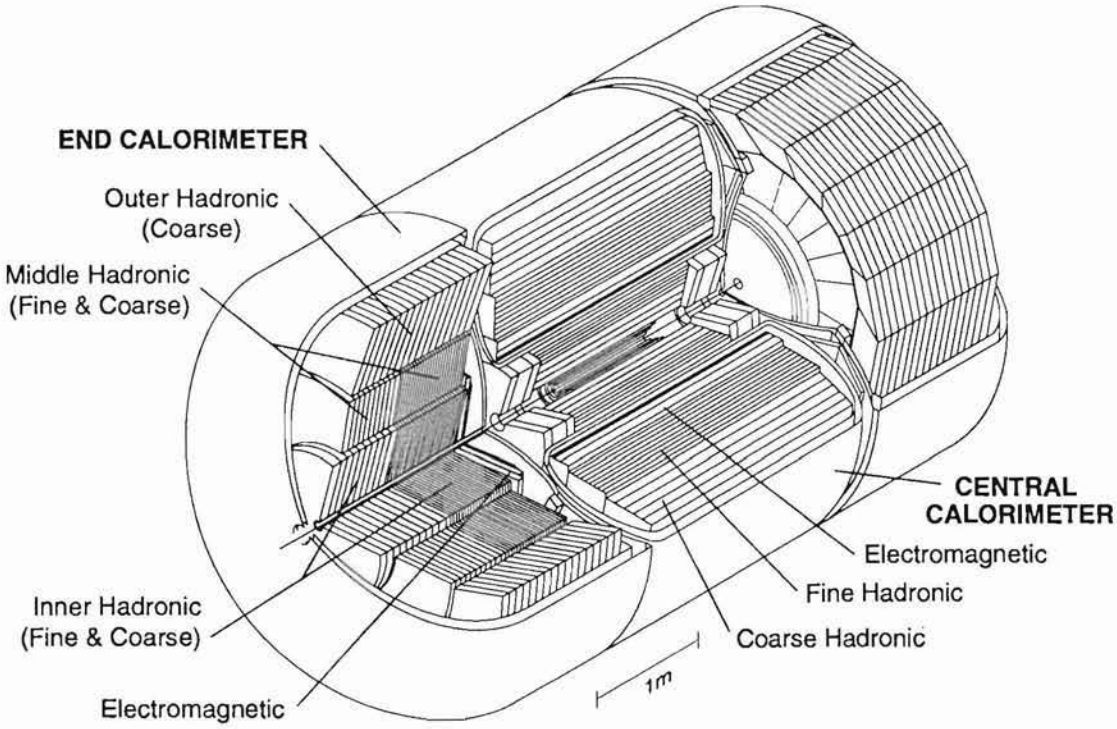

Figure 6: The DØ calorimeter system.

Electromagnetic (CCEM), Fine Hadronic (CCFH) and Coarse Hadronic (CCCH). The CCEM layer has relatively thin uranium plates in 32 modules. The CCFH layer has somewhat thicker uranium plates in 16 modules. The CCCH uses thick copper or stainless steel plates in 16 CH modules. These are illustrated in Fig. 7. From a basic cell structure, the calorimeter is built up into a set of pseudo-projective readout towers with each tower subdivided in depth. Individual towers

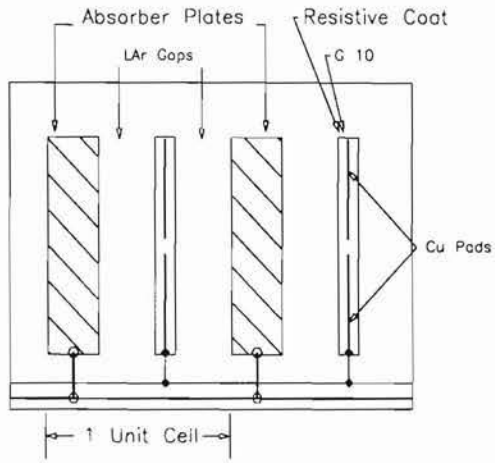

Figure 7: Unit cell in the DØ calorimeter.

in the central region span $\Delta\eta = 0.1$ and $\Delta\phi = 0.1$.

The CCEM has four layers in depth. The first two, totaling 2 X_0 (radiation lengths) in thickness, are for sampling longitudinal shower development near the beginning of showers, where γ's and $e^{\pm}$'s shower differently. The third layer includes the region of maximum EM shower energy deposit and is 6.8 X_0 thick. The fourth layer is 9.8 X_0 thick and makes the total thickness for the CCEM approximately 20 X_0. The third layer of the CCEM is twice as finely segmented as usual in both η and ϕ for better determination of EM shower centroids. The modules span 24 $\Delta\eta = 0.1$ towers for a length of 260 cm. A full module comprises 20.5 X_0 and 0.76 λ_A (nuclear absorption lengths).

The Fine Hadronic part of the calorimeter has three layers with thicknesses of 1.3, 1.0, and 0.9 λ_A. The Coarse Hadronic part has one layer 3.2 λ_A thick. Including support structures, the Central Calorimeter weighs approximately 305 metric tons and contains an additional 26 metric tons of Liquid Argon.

Table 4: Central Calorimeter characteristics

Central Calorimeter	EM	FH	CH
Number of modules	32	16	16
Absorber [a]	Uranium	Uranium	Copper
Absorber Thickness (cm)	0.3	0.6	4.65
Argon gap (cm)	0.23	0.23	0.23
Number of signal boards/module	21	50	9
Longitudinal depth	20.5 X_0	3.2 Λ	3.2 Λ
Number of readout layers	4	3	1
Number of signal boards/readout depth	2,2,7,10	21,16,13	9
Total X_0 [b]	20.5	96.0	32.9
Total λ [c]	0.76	3.2	3.2
Sampling fraction (%)	11.79	6.79	1.45
eadout segmentations ($\Delta\phi \times \Delta\eta$) [d]	0.1×0.1	0.1×0.1	0.1×0.1
Total number of readout cells	10368	3000	1224
Maximum pseudorapidity coverage	± 1.2	± 1.0	± 0.6

[a] Uranium absorbers are depleted. FH absorbers are alloy of Uranium and 1.7% of Niobium

[b] Total radiation lengths at $\eta = 0$

[c] Total interaction lengths at $\eta = 0$

[d] The third layer of the EM calorimeter is 0.05×0.05 in $\eta - \phi$ space.

The energy resolution of a sampling calorimeter can be expressed as:

$$(\frac{\sigma_E}{E})^2 = C^2 + \frac{S^2}{E} + \frac{N^2}{E^2}$$

where E is the energy of the incident particle, C is a constant reflecting calibration errors, S represents fluctuations in the LAr gaps, and N is a constant representing electronic noise and the natural radioactivity of the uranium absorber. Measured in test beam studies [21][22] the values used for the CC were $C = 0.0 \pm 0.005$, $S = (0.81 \pm 0.016)\sqrt{\text{GeV}}$, and $N = 7.07 \pm 0.09\text{GeV}$. Further characteristics of the Central Calorimeter are listed in table 4[23].

4.2.1 Massless Gaps and The ICD

Because of support structures, the region $0.8 < |\eta| < 1.4$ has less calorimeter absorber than the central or end regions. To provide calorimetric coverage in these regions, two types of detector have been installed. One is the Intercryostat Detector (ICD) and the other is the Massless Gaps Detector (MGD)

There are two ICD's, one mounted on each of the two end calorimeters. Each ICD consists of an array of 384 scintillator tiles covering $\Delta\eta = \Delta\phi = 0.1$, the same as the calorimeter cells. These form a pseudo-projective structure with the calorimeter cells. The ICD uses phototube readout.

The MGD's are mounted on the CCFH, ECMH, and ECOH modules. The MGD's are single cell structures consisting of two signal boards surrounded by three LAr gaps. These cells are the same size as the ICD and calorimeter cells and are used in the readout like the ICD and Calorimeter cells.

4.3 DØ Muon System

The muon detector system (Fig. 8) provides nearly complete coverage in the region $|\eta| < 3.4$. There are three detector sections covering different ranges in pseudo-rapidity. The Wide Angle Muon System or WAMUS covers $|\eta| < 1.0$, the End cap toroids or EF covers $1.0 < |\eta| < 2.5$ and the Small Angle Muon System or SAMUS covers $2.5 < |\eta| < 3.6$. Separate magnetized iron toroids are employed in each section. The Central toroid or CF is made up of three parts: The bottom is fixed to the detector platform and helps provide support for the Trackers and Calorimeter. The other two parts are shells which can be pulled apart to allow access to the inner detectors. A magnetic field of 1.9 Tesla is generated by

twenty coils of 10 turns each carrying 2500 Amps. There are 164 WAMUS and EF chambers and 6 SAMUS stations. Fig. 9 shows that the thickness of the detector

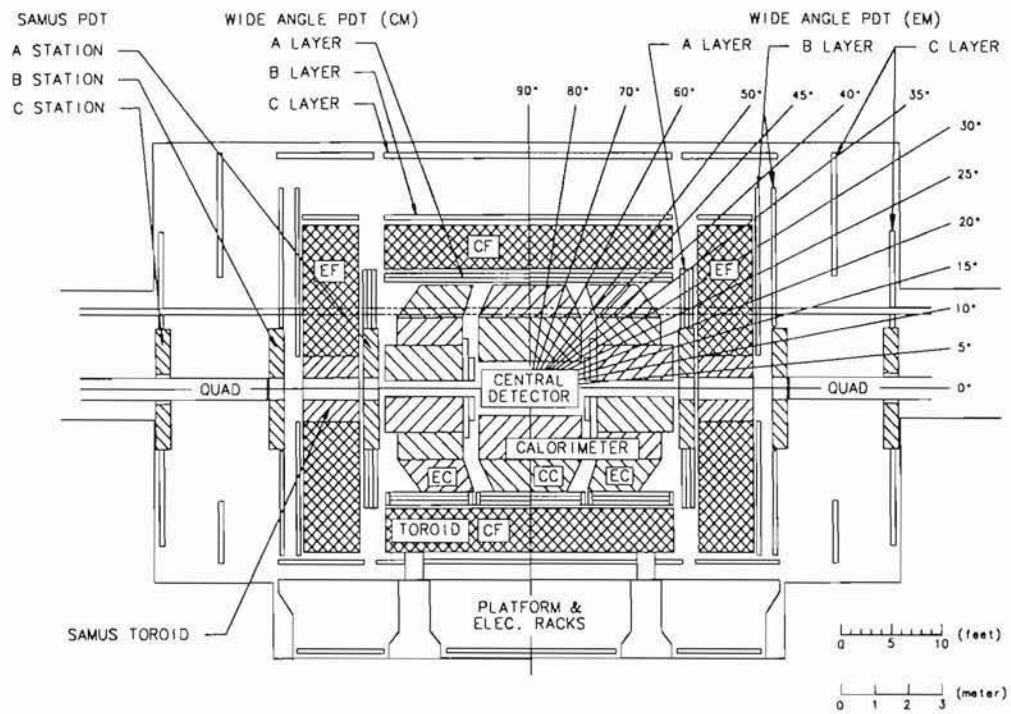

Figure 8: Elevation view of the DØ detector.

ranges from 8 λ near the CF-EF boundary to a maximum of about 20 λ in the EF region. This means that the minimum muon momentum required to traverse the toroids ranges from 3.5 GeV/c at $\eta = 0.0$ (in the CF) to about 5 GeV/c in the EF. WAMUS contains three layers of muon chambers with a magnetized iron toroid (CF). The 'A' layer muon chambers are situated just outside the Calorimeter and inside the CF toroid. Beyond the toroid are the B and C layers.

Muon chambers are proportional drift tube (PDT) cells [25] arranged in decks to form layers. The A layer chambers have four decks while the B and C layer

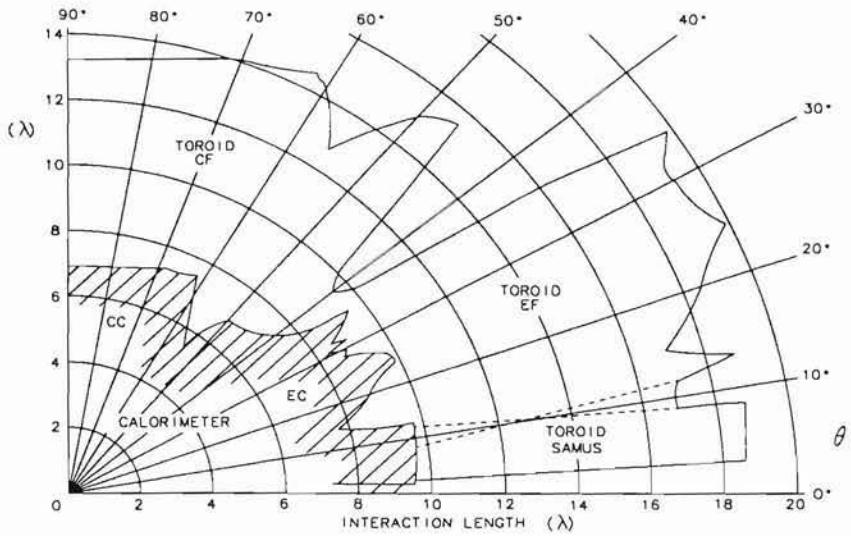

Figure 9: Total interaction lengths of calorimeter and muon system.

chambers have three decks each.

The PDT cells are composed of etched cathode pad strips on the top and bottom with gold-plated tungsten anode wires through the middle of each cell. The cathode pads are etched in a repeating diamond pattern with a 61 cm cycle. Between cells of different decks the pattern is offset. The maximum drift distance across the cell is 5 cm. The aluminum cell walls in the chambers are grounded while the cathode pads are held at +2.3 kV and the anode wires are held at +4.56 kV. The gas mixture was $Ar(90\%)CF_4(5\%)CO_2(5\%)$ with a drift velocity of 6.5 cm/μs near the wire but dependent on the changing $\vec{E}$ across the cell (see fig. 10). An approximately linear time-distance relation was found with this configuration. Pairs of PDT cells are read out using Time to Voltage converters (TVC's) giving drift times, for a drift coordinate, and delta-times which give an estimate for position along the wire with a resolution of between 10 and 20 cm.

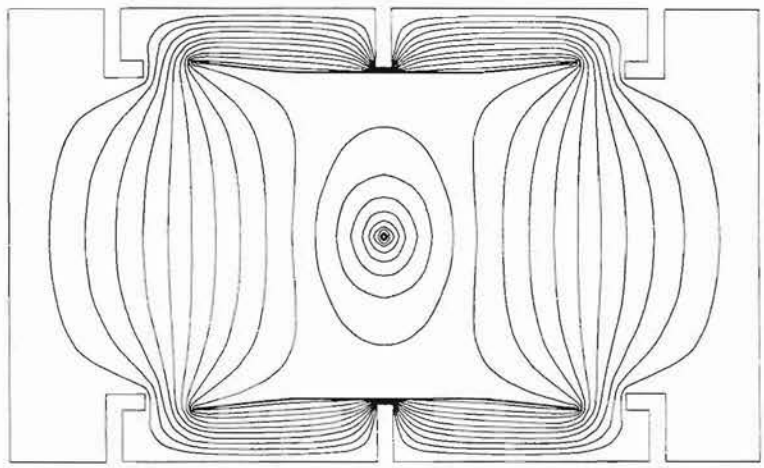

Figure 10: Equipotential lines of a muon PDT cell ; signal wire at +5 kV, vernier pads at +2 kV.

Finer determination of the coordinate along the wire is given by the ratio between image charges (from the cascade deposited on the wire) on the inner and outer sections of the etched cathode pads of the PDT cathodes. From the drift velocity and drift time the drift distance is determined and, because of the orientation of WAMUS chambers about the central region, this gives the bend coordinate. Bend coordinates are determined with a resolution of near 500 μm. while coordinates along the wire are determined with a resolution of approximately ± 3 mm. Each WAMUS chamber has a set of electronics boards housed in enclosures attached to the chamber body. ADCs and Trigger electronics reside in the Moveable Counting House (MCH). Between layers cells are staggered to reduce ambiguities in solutions for drift coordinates. The third coordinate of the hit point is given by the location of the deck in the hit layer. Tracks are constructed from hits in A + B + CC layers,

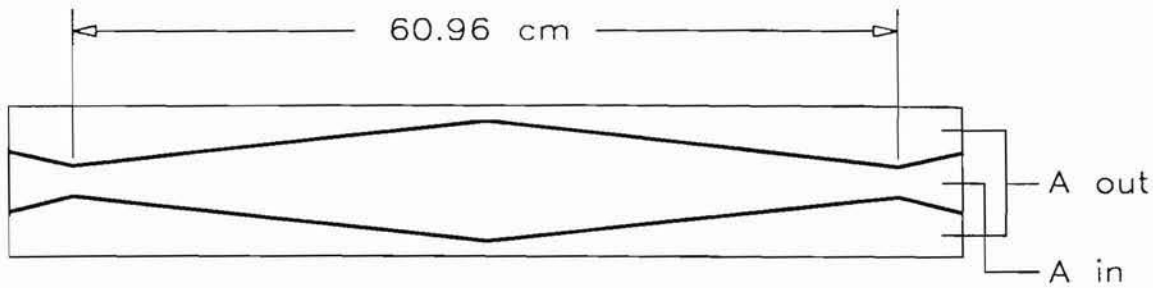

Figure 11: WAMUS PDT cathode pad structure.

in A + B or in A + C layers . Additional information is obtained from matching track candidates in the muon detector to track segments in the Central Tracker. This reduces the uncertainty of the track segment inside the toroid because of the spread of the interaction region (width $\sigma_z \approx 30$cm).

The bending the μ undergoes through the magnet toroid (radial magnetic field $\vec{B} = B_0\hat{\phi}$) determines the muon momentum. Momentum determination for low momentum muons is limited by multiple Coulomb scattering to a resolution of $\Delta P/P \geq 18\%$. Some characteristics of the DØ muon system are listed in table 5

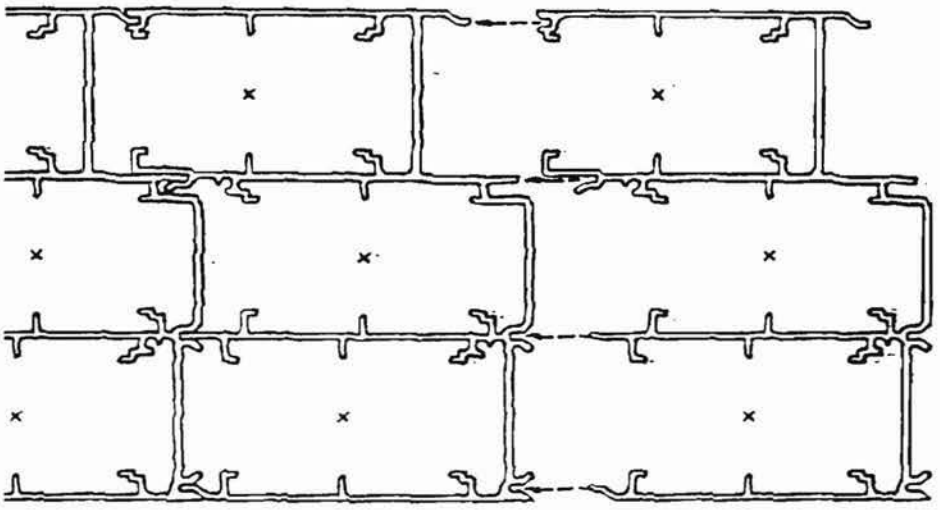

Figure 12: B or C layer muon chamber

Table 5: Design parameters of the DØ muon system

Magnetic field strength	1.9 T
Magnetic kick (90°)	0.61 GeV/c
Design resolution in bend plane	500 μm (Diffusion limit, 200 μm)
Design resolution in non-bend plane	2-3 mm[a]
$\delta p/p$ (multiple scattering limit)[b]	18%
3σ sign determination ($\theta = 90°, \phi = 0°$)	$P_t \leq$350 GeV/c
Interaction lengths (90°)	13.4
Interaction lengths (5°)	18.7
Drift-coordinate resolution	±0.45 mm

[a]Taking charge ratio known to within 1% absolute

[b]Theoretical upper limit assuming 100% chamber efficiency.

5 DATA SET

5.1 Trigger and Data Acquisition

At an operating lumninosity of $5 \times 10^{30}\text{cm}^{-2}\text{sec}^{-1}$ the collision rate is around 100 kHz. The DØ detector system is able to acquire and write to tape only about 2 Hz. To select interesting physics events, a multi-level triggering scheme was developed [26] which coordinates output from the different detector subsystems.

Some initial signal processing (shaping, zero supression and fast ADC) takes place at the chambers with the resulting information immediately available for hgher levels of trigger determination. In some cases it is possible to make a higher level decision within the time between beam crossings (3.5 μs) while in other cases several beam crossings take place before a decision can be made on whether or not to trigger on the event.

Triggering on characteristics of the total event, combining the results of decisions made on output from different subsystems, occurs at the highest level of the trigger.

The following briefly describes each level in the trigger scheme of the DØ detector (see Fig. 13).

5.1.1 The Level 0 Trigger

The Level 0 trigger is a fast hardware trigger on inelastic collisions in the D0 detector. It makes a fast measure of the interaction vertex using the firing time difference of the scintillator hodoscopes, and also serves as the luminosity monitor for D0 [27]. The hardware for this trigger consists of two scintillator hodoscopes, each mounted on opposite sides of the central tracker and along the beam axis.

The time resolution of the hodoscopes is typically 100-150 ps.

The Level 0 calculations are performed in hardware and are available for Level 1 and Level 2 trigger decisions. The rate of Level 0 triggers is about 150 kHz at a luminosity of $5 \times 10^{30} \mathrm{cm}^{-2} \mathrm{s}^{-1}$.

5.1.2 Level 1 and 1.5 Triggers

The Level 0, Level 1 and Level 1.5 are hardware triggers run by a flexible software architecture. There are 32 possible hardware triggers, each of which is a logical combination of 256 input terms which include information from Level 0, from the accelerator or from centroids read out from the calorimeter or muon system (see Fig. 14). The Level 0 and Level 1 triggers operate within the 3.5 μs window between beam crossings in 135 ns steps. Additionally, for the muon system there's an another level of hardware trigger (Level 1.5) which incurs some deadtime because it takes longer than the 3.5 μs window, but improves the spatial resolution of candidate triggering muons from 60 cm to 5 cm. The muon Level 1 trigger is called the Coarse Centroid Trigger and the Level 1.5 muon trigger is called the Octal Centroid trigger. The output from Level 1.5 is the number of muon candidates above some muon P_t threshold in different geographical regions of the detector. The output rate from Level 1 triggers is approximately 200 Hz and the rate from level 1.5 is about 100 Hz.

5.1.3 The Level 2 Trigger

The Level 2 Trigger is a software trigger. It uses FORTRAN filtering code running in 32 VAX 4000/60 microprocessors that operate in an ELN system. For each hardware trigger satisfied, a sequence of 'filter tools' is run which refine the

hardware trigger decision by using information from the whole detector. Number of jets, missing E_T and scalar E_T are some of the criteria used in Level 2 triggers. There is also the capability to trigger on event topology in multi-jet, muon plus jet and other interesting events. The ability exists in Level 2 to make an initial survey of calorimeter cells with signals above the pedestal.

The maximum input rate to the Level 2 system is 200 Hz. The output from Level 2 is limited to approximately 2 Hz which is the maximum rate at which events can be written to tape.

5.1.4 Calorimeter Triggers

The data used for the analysis in this thesis satisfied one or more of four Calorimeter triggers (see table 6). The calorimeter trigger involves two parts which are the global and cluster parts [28]. In the global part, overall transverse energy is summed :

$$E_t = \sum_{i=1}^{nfired} \left[E_t^{EM}(i) + E_t^{HAD}(i) \right]$$

In the cluster part, trigger towers are formed by grouping cells by $\Delta\eta \times \Delta\phi = 0.1 \times 0.1$ and in depth, forming semi-projective towers. Clustering is performed in Level 2 while the global determination is made in Level 1.

5.2 Offline Jet and Muon Reconstruction

5.2.1 Jet Reconstruction

The definition used here for a jet is that the sum of transverse energy in calorimeter towers contained in a cone of size R exceeds some threshold value. Calorimeter towers are determined with respect to the vertex, found from tracking.

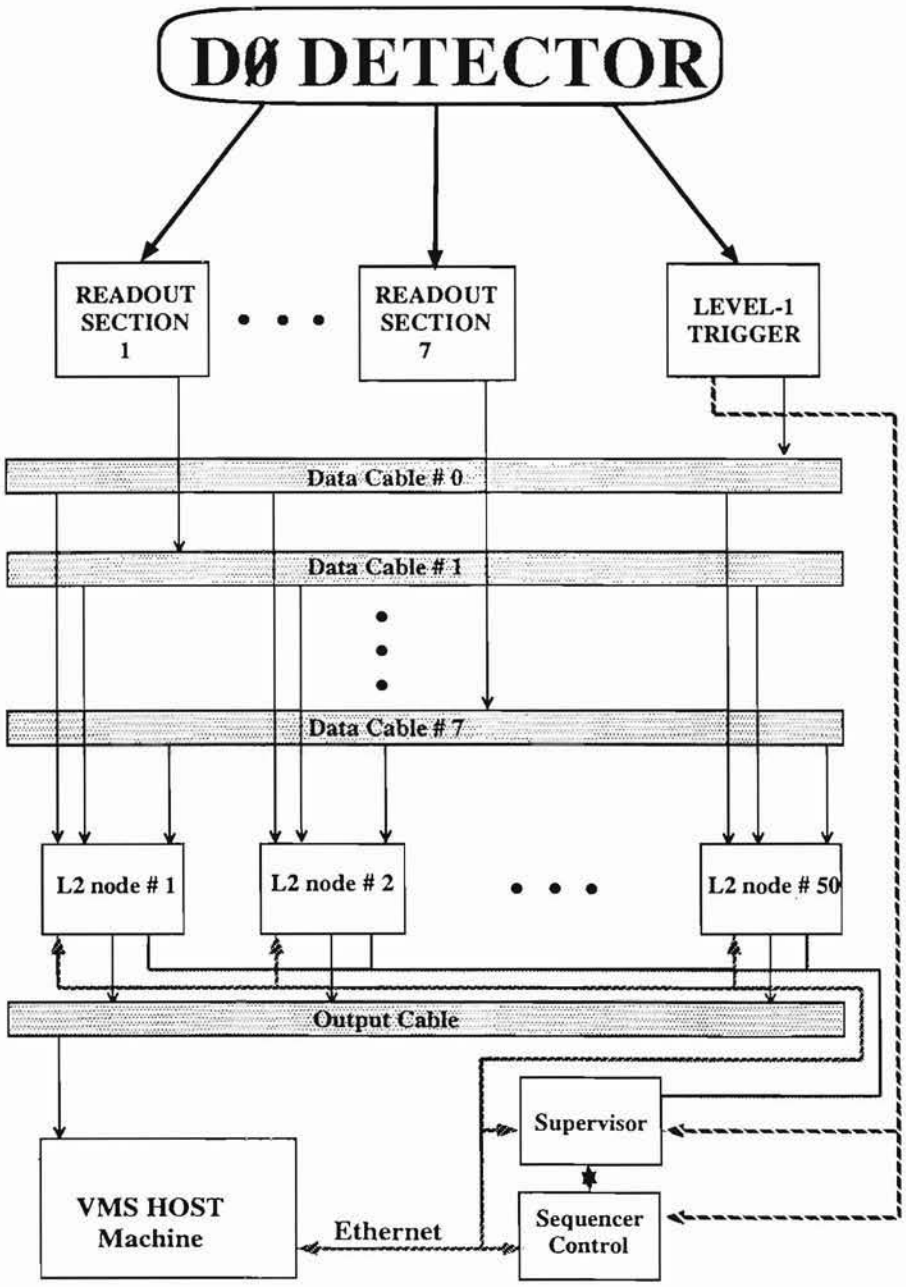

Figure 13: DØ Trigger and Data Acqusition System.

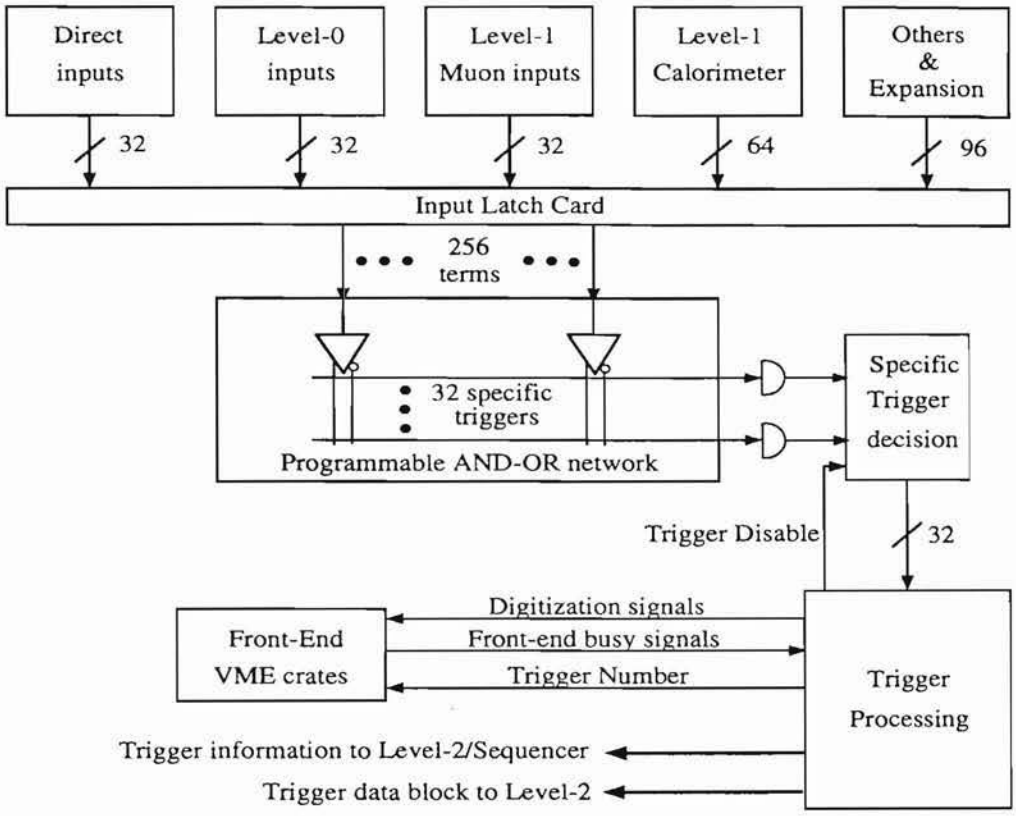

Figure 14: Level 1 Trigger processing stages

Table 6: Level 2 terms used in data selection

L2 trigger			$\int \mathcal{L}dt\,(\mathrm{nb}^{-1})$
L2bit	Name	Requirement[a]	
18	jet_min	$E_t > 20$	5.5359
18	jet_low	$E_t > 30$	80.3354
19	jet_med	$E_t > 50$	703.064
20	jet_high	$E_t > 80$	5601.63
21	jet_max	$E_t > 115$	9555.02

[a]For one jet in event, in Δ R = 0.7 cone using L2 information.

Within the cone, $\Delta R = \sqrt{(\eta_j - \eta_t)^2 + (\phi_j - \phi_t)^2}$ with (η_t, ϕ_t) being the center of a calorimeter tower, the jet direction is defined to be:

$$\eta_j = -\log\left(\tan\theta_j/2\right)$$

$$\phi_j = \tan^{-1}\left(\frac{\sum_i E_{yi}}{\sum_i E_{xi}}\right)$$

and

$$\theta_j = \tan^{-1}\left(\frac{\sqrt{\sum_i E_{xi}^2 + \sum_i E_{yi}^2}}{\sum_i E_{zi}}\right)$$

where

$$E_{xi} = E_i \sin\theta_i \cos\phi_i$$

$$E_{yi} = E_i \sin\theta_i \sin\phi_i$$

$$E_{zi} = E_i \cos\theta_i$$

with i referring to the ith tower contained by the cone. The transverse energy of a jet is defined to be:

$$E_T = \sum_i E_{Ti}$$

and

$$E_{Ti} = E_i \sin\theta_i$$

The algorithm used to find jets starts by looking for 'seed' towers with energy 1.0 GeV above pedestal. Pre-clusters are next formed by summing towers within $R \leq 0.3$ of the seed tower. Then all towers about the centroid of this precluster within the final cone size (typically 0.3, 0.5 or 0.7 with 0.5 used in this analysis) are summed and the jet center is determined according to the definition:

$$\eta_j = \frac{\sum_i E_{Ti}\eta_i}{\sum_i E_{Ti}}$$

and

$$\phi_j = \frac{\sum_i E_{Ti}\phi_i}{\sum_i E_{Ti}}$$

The preceding steps are iterated until stable jets are found. In this analysis jets with $E_T \geq 10$ GeV are kept for analysis.

5.2.2 Muon Reconstruction

The muon chambers are arrays of proportional wire chamber cells with signal readout from pairs of adjacent cells (in almost all cases - there are a few exceptions). Two coordinates for a track candidate hit are determined in the plane of the chambers with the third coordinate given by the location of the chamber. In the plane are the drift coordinate, the distance between the muon track and the anode wire, and the wire coordinate, the position along the wire.

In the central region the drift wires are perpendicular to the beam axis so that deflections of charged particles traversing the magnet toroid are observed in the 'drift' coordinates from hits in these chambers. Ionization caused by a charged particle traversing a cell results in charge deposition on the wire which induces an image charge on the cathode pad. This sets a pad latch. Pad latch bits indicate which cell of the pair is hit (cell pairs have an even and odd cell) and the drift time is checked to determine if it is 'physical' (in time with a beam crossing).

Drift times are corrected for drift velocity and time of flight (the time it would take a particle from the interaction point to reach the muon chamber). This fixes the distance from the wire for a hit coordinate. At this point in the processing an ambiguity exists as to whether the coordinate is on one side of the wire or the other. The two solutions are considered as separate coordinates for the time

being.

The time difference between the signal read out at one end of the cell pair and the other gives a delta-time. For a particular cell pair this delta-time indicates which cycle in the diamond pattern (etched on the cathode pads) contains the hit. Taking the charge ratio between inner and outer cathode sections gives the coordinate along the wire.

From the drift, wire and chamber coordinates, points are arranged in two projections called bend and non-bend views. In the non-bend projection points are considered between A and B and/or C layer muon chambers in a straight line through the magnet. In the bend-view projection, track segments in the A layer are matched with segments in the B and/or C layers, with the constraint that the segments match in the middle of the magnet. In this case the drift coordinates with the best fits are kept and the ambiguity previously described is removed.

The first segments checked are the BC layers in the bend view. A minimum of 4 planes (out of 6 total) in these layers are required to have hits, and one hit per plane is considered. Next a search is made for a matching A-layer segment. The A-layer segment requires at least 2 hit planes (out of 4 total), with the interaction vertex inside and the BC segment (projected to magnet center) outside these hits providing additional reference points.

From the best fit in the bend view and by knowing the magnetic field strength in the toroid, the muon momentum is determined. From results of the muon system track fit, quality flags are set for the quality of fit in each view, the quality of track projection through the vertex, and the value of $\int \vec{B} \cdot d\vec{l}$, to indicate the goodness of the muon momentum determination.

Lastly, a global fit is evaluated for muon candidates. This uses information from the Calorimeter and Central Detectors together with the information from the Muon system. From the vertex measurement Y and Z coordinates are used with four points from the Central Detector to give bend and non-bend track segments. Angle measurements between the CD track segment and the muon track segment indicate the amount of multiple Coulomb scattering in the Calorimeter. The energy in the calorimeter along the muon track is measured and compared to the expected energy deposition for a traversing muon. Finally, the muon track segments themselves are used. There are a total of 16 measurements considered and the algorithm performs a χ^2 fit in terms of seven global parameters: four muon track parameters in the CD, two Coulomb scattering parameters in the Calorimeter and one parameter from the inverse muon momentum, $1/p_\mu$.

5.3 Event Selection

From the entire data set of those events satisfying any of the jet triggers, events were selected in which the two highest E_T jets were contained in the CC, $|\eta_j| < 0.6$. Jets were determined using a cone algorithm with reference cone size $\Delta R = 0.5$. This cone size was chosen so that wholly contained (by the jet ΔR cone), clearly separate jets with substantial parton energy are selected. This minimizes the background of fake jets from calorimeter fluctuation while detecting the hard scatter of partons from the $p\overline{p}$ interactions.

Events with two central jets are called $2 \rightarrow 2$ process candidates. Among these events a search was conducted for muons associated with either of the jets. The criteria for association between muon and jet was that muons are within ΔR of

0.5 of the jet. In addition to the η requirement, jets were required to satisfy the following criteria :

- Fraction of jet energy in EM is $5\% \leq$ EMfract $\leq 95\%$.
- Fraction of jet energy in Coarse Hadronic $\leq 40\%$.
- Ratio of hottest cell in jet to next hottest cell is $< 10 : 1$.
- Two highest E_T jets have $|\eta_J| \leq 0.6$.
- Jet $E_T \geq 10$ GeV.

The first three are for verifying that the profile of the reconstructed jet energy in the calorimeter was more like a real jet than a fake one due to calorimeter energy fluctuations and the fourth requirement is to ensure a reasonably high reconstruction efficiency. Associated muons were required to satisfy the following criteria :

- $|\eta_\mu| \leq 1.0$.
- Δ R between μ and Jet < 0.5.
- At least two muon chamber layers used in μ fit.
- Path through the toroid, $\int \vec{B} \cdot d\,\vec{l} \geq 0.6$.
- $|T_0| \leq 200$ ns.
- $P_T^\mu \geq 4.0$ GeV/c.

The η cut was imposed to keep central muons because muon detection and reconstruction efficiency were optimised in the central region. The $\Delta - R$ cut was to ensure clear association between the muon and jet. The third requirement was to ensure the muon had been well detected by the muon system. The fourth requirement was to ensure optimum momentum determination. The fifth requirement was to ensure the muon track was consistent with the time of beam crossing and time of flight estimated for the muon in order to eliminate the background from cosmic rays. The last requirement was to select muons with enough momentum to exit the calorimeter and iron absorber.

Characteristics of accepted muons and jets are shown in Fig. 15. The E_T balances of all two, three and four jet events from the set satisfying the calorimeter triggers are shown in fig. 16. The total transverse energy in these events is mostly contained by the jets, indicating that single, well contained and reconstructed hard-scatterings have occurred. Here 'balance' is defined to be:

$$\text{Balance} = \left| \frac{\sum_{jets} \vec{E}_t}{\sum_{jets} |\vec{E}_t|} \right|$$

Figures 17 thru 21 are examples of two and three jet events as reproduced in the DØ event display. All selected events events were very clean with clearly isolated jets and insignificant calorimeter background activity. Muons are clearly contained by the associated jets and the overall missing E_T for these events was in the vicinity of the associated μ + jet, indicating well contained and reconstructed events.

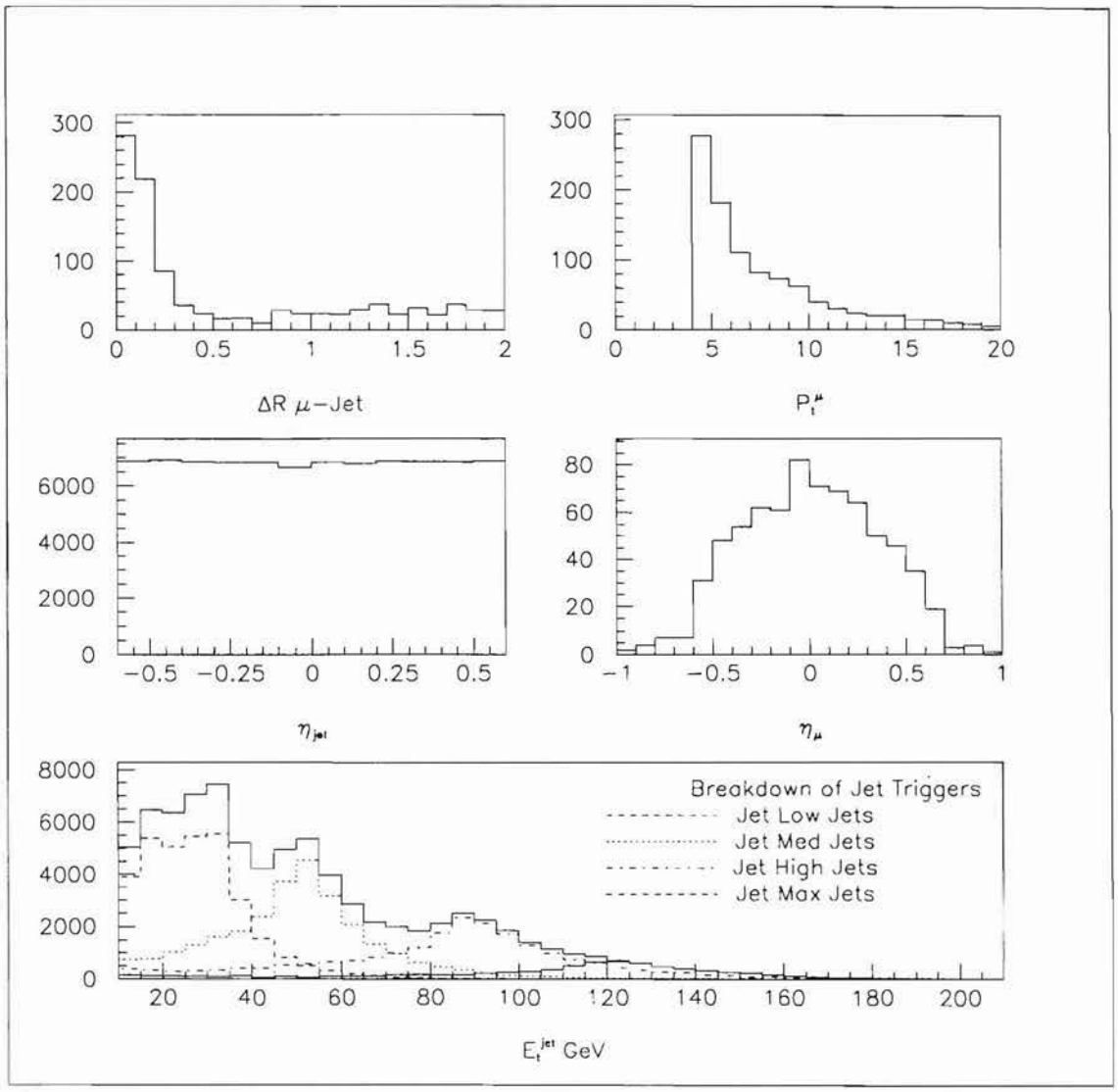

Figure 15: Characteristics of the data set

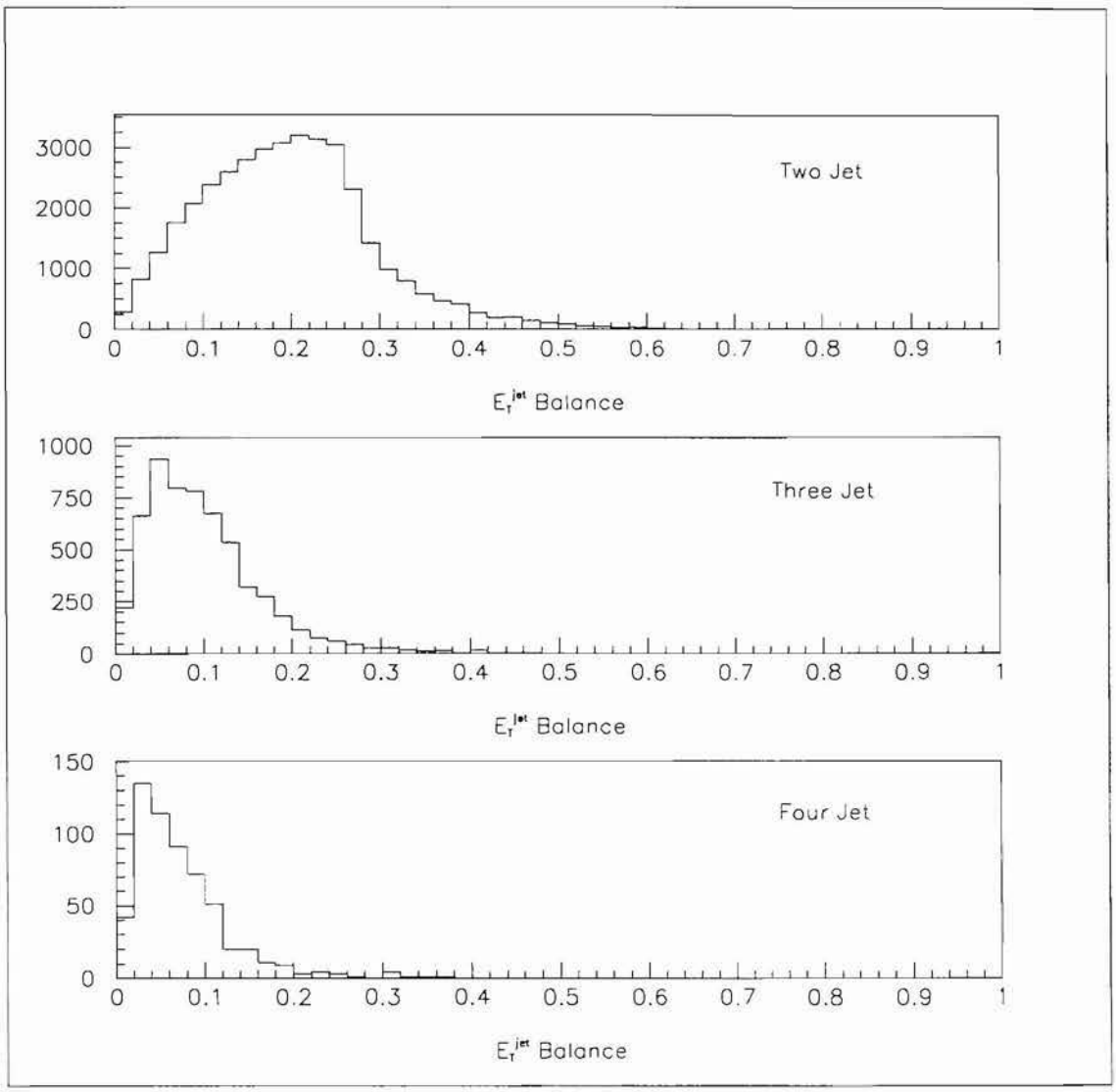

Figure 16: Jet E_T Balance of n-jet events selected

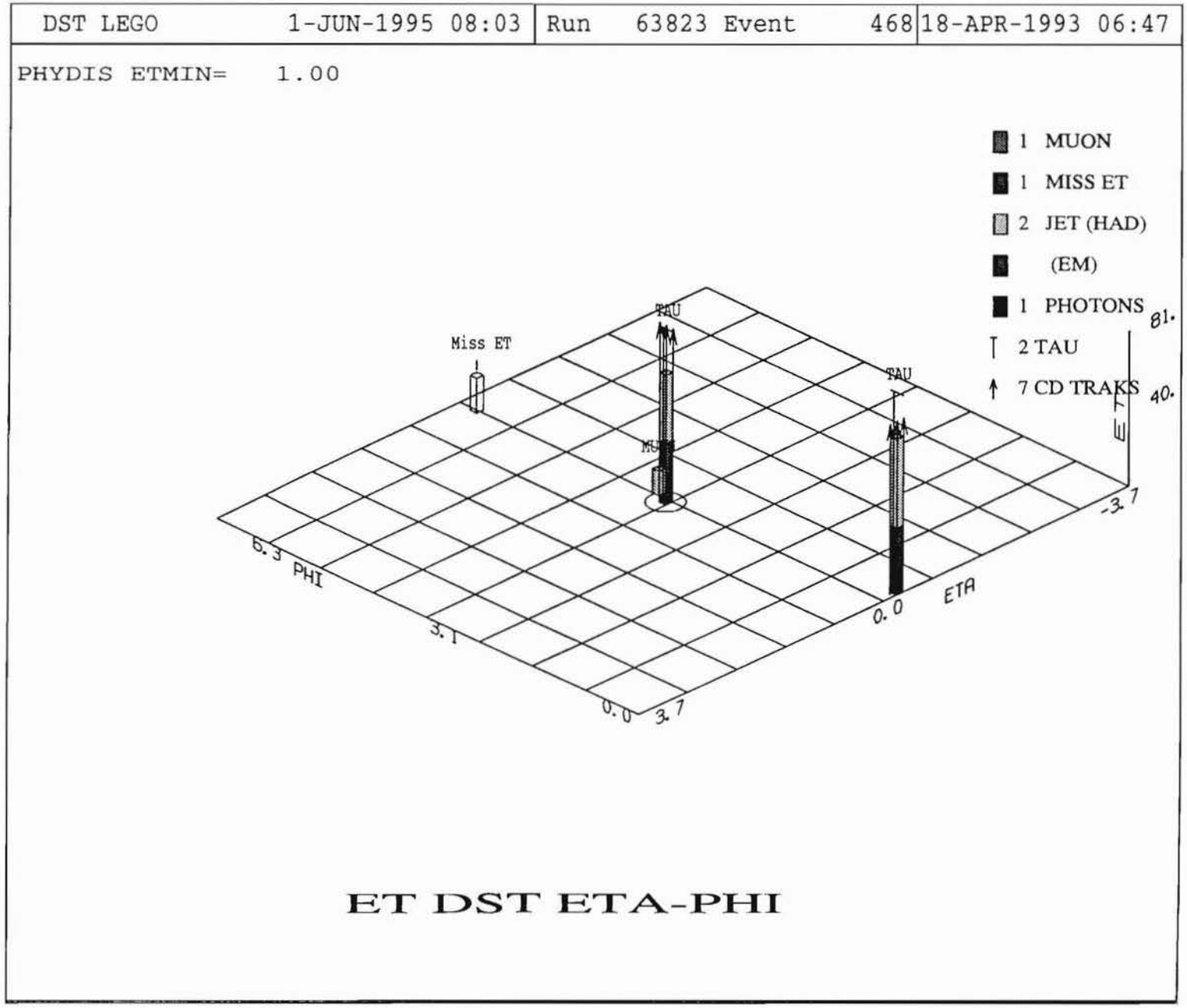

Figure 17: Lego plot of a typical Two Jet Event

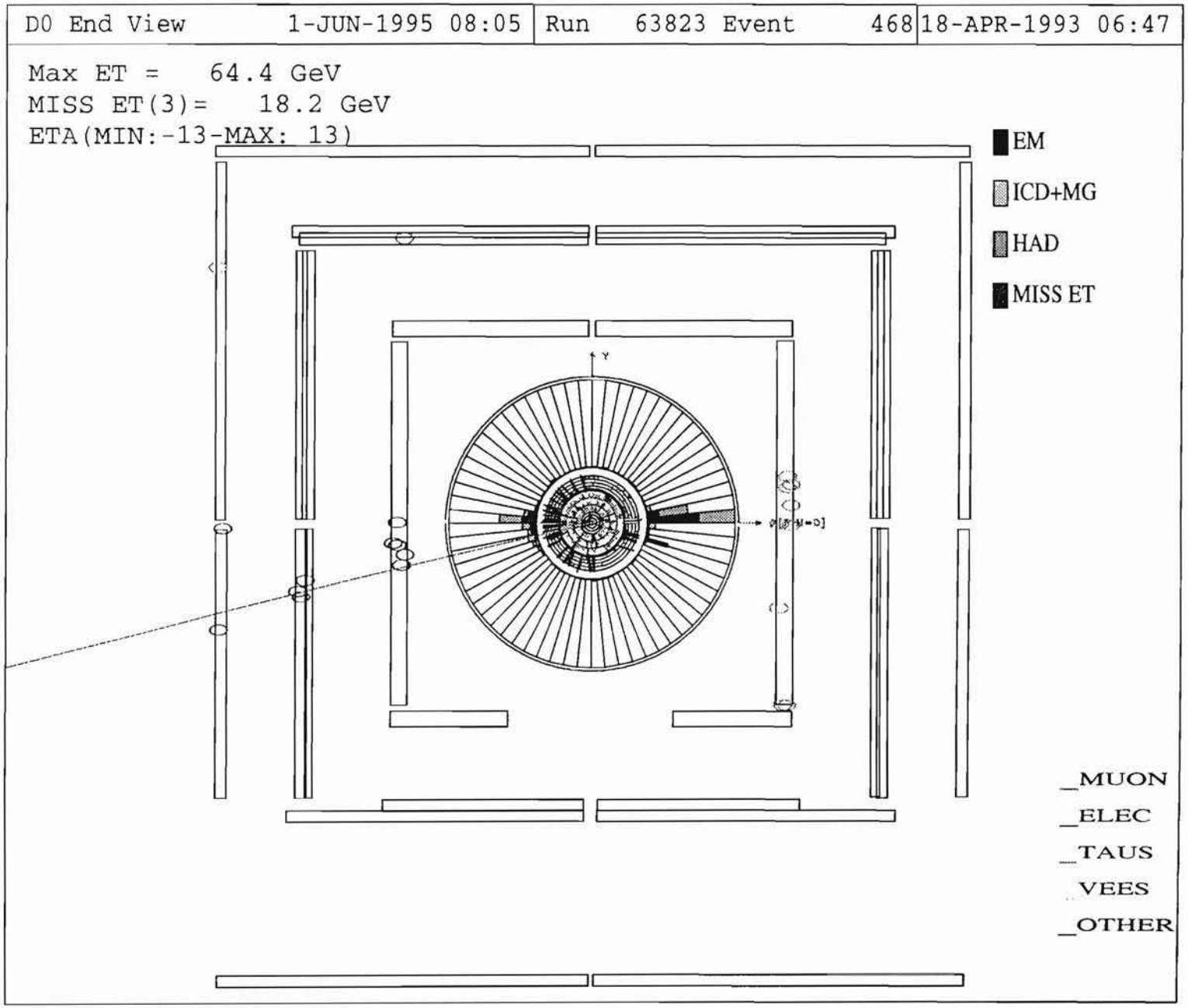

Figure 18: End view of a typical Two Jet Event

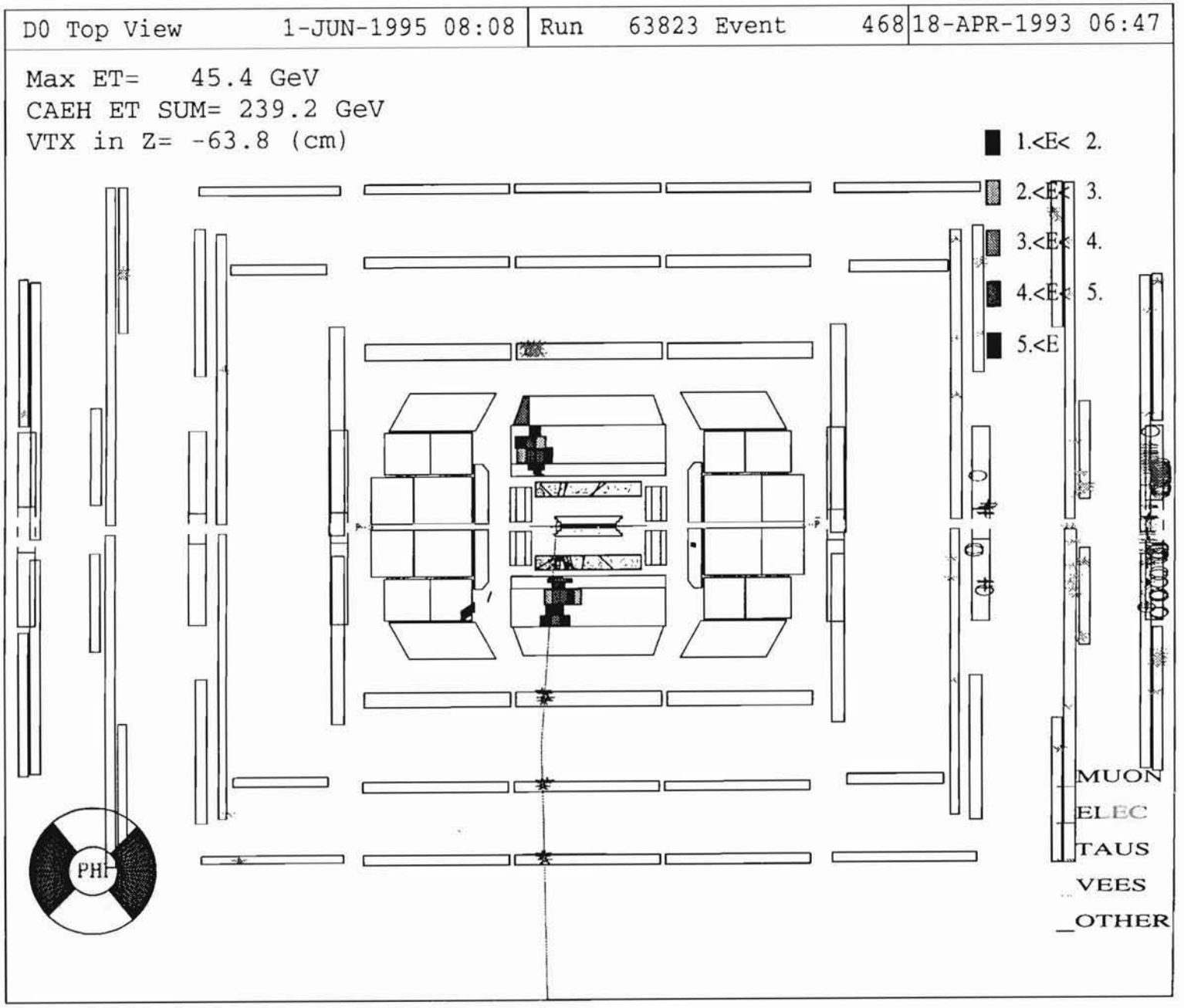

Figure 19: Top view of a typical Two Jet Event

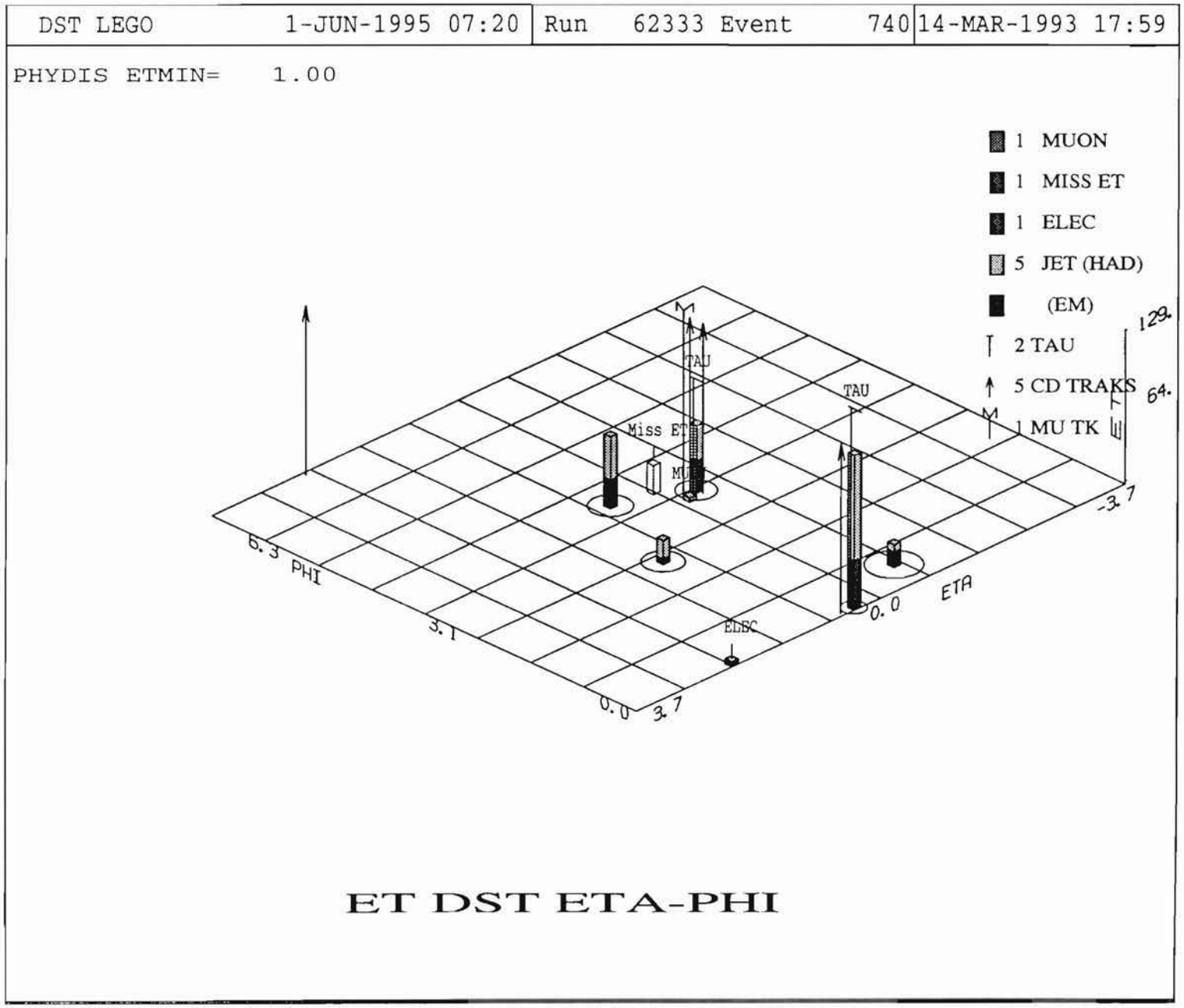

Figure 20: Lego plot of a typical Three Jet Event

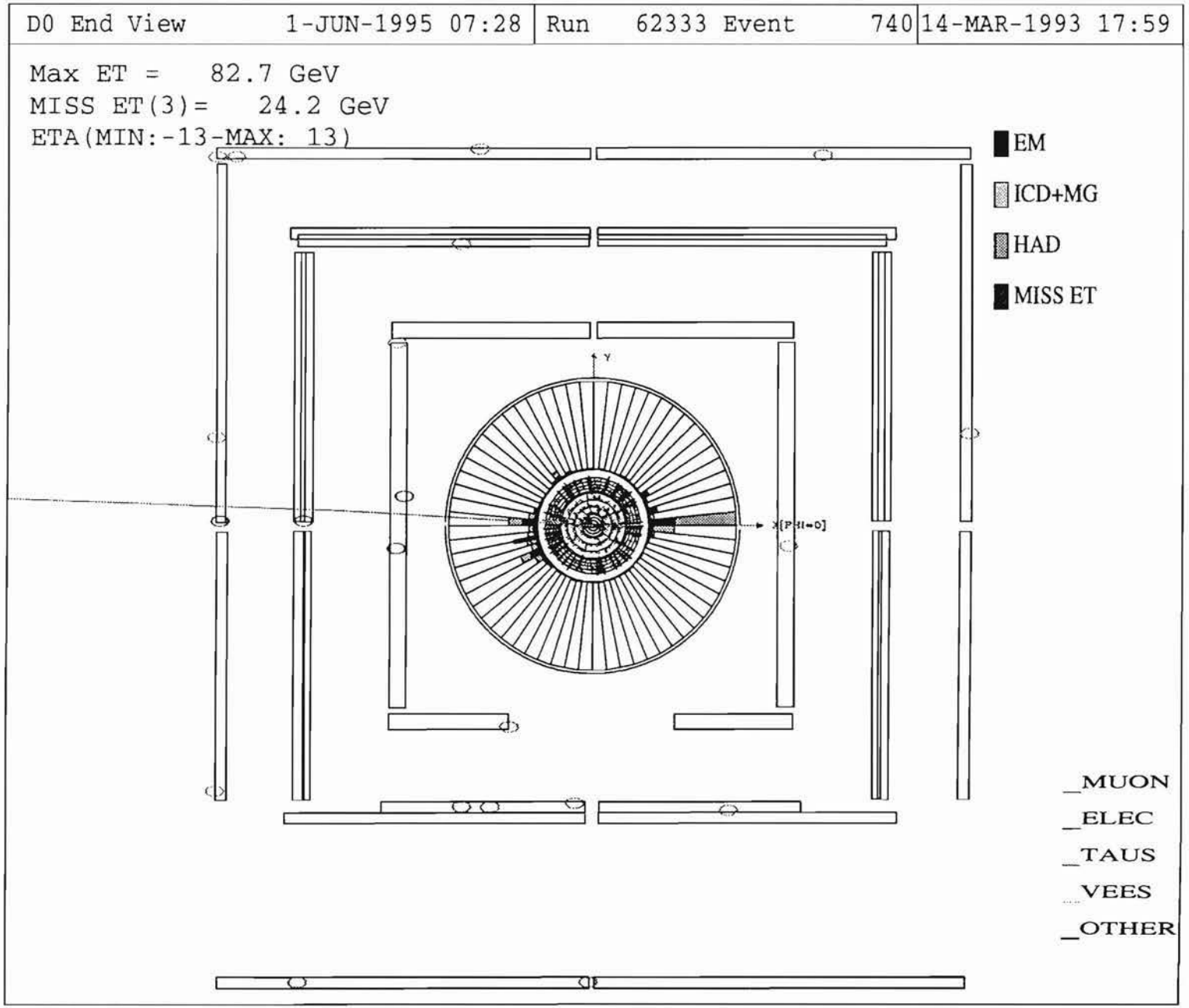

Figure 21: End view of a typical Three Jet Event

6 ANALYSIS OF THE DATA SET

6.1 Approach

This thesis investigates the production of bottom (beauty) and charm quarks in QCD jets at the DØ detector at Fermilab. The amount of gluon splitting into heavy quark pairs in QCD jets is measured and compared to an analytic expression derived by Mangano and Nason [24] for the amount of perturbative gluon splitting into heavy quark-antiquark pairs. If the observed production of heavy quark pairs significantly exceeds this prediction it could indicate that non-perturbative effects or higher orders in α_s are important.

Events are selected where the two highest E_T jets are in the central region of the detector ($|\eta_{jet}| < 0.6$). This makes possible the estimation of the total number of gluon jets in the sample from leading order perturbative QCD. Different structure functions are used in the Monte Carlo generator to estimate systematic uncertainty in the estimation of total number of gluon jets.

In the two-jet events a search is made for muons associated with either jet. To determine the fraction of these muons coming from quarks that are from gluon splitting and the fraction of muons from quarks that are from direct production, $2-D$ likelihood fits are made to the P_T^{rel} vs $Z_{\|}$ distributions of the data. By taking into account the branching ratio for b and c quarks to decay to muons and taking into consideration the muon reconstruction efficiency, the total number of quark pairs ($b\bar{b}$ and $c\bar{c}$) from gluon splitting is determined. Ratios for the number of quark pairs from gluon splitting to the number of gluon jets are calculated by dividing the number of quark pairs by the estimated number of gluon jets in the inclusive jet sample. These ratios are then compared with analytic estimates

made by Mangano and Nason.

6.2 Monte Carlo

The Monte Carlo model is used to:

- Estimate the rate and characteristics of μ's from π and K decays in jets.
- Model the characteristics of μ's from heavy quark decays when the heavy quarks are from gluon splitting.
- Estimate the number of gluon jets in the sample.

The Monte Carlo model used here is Herwig (version 58) which is based on the Lund string fragmentation model [29].

6.2.1 $\pi^{\pm}$ and $K^{\pm}$ Decay Estimates

To generate the characteristics of μ's from $\pi^{\pm}$ and $K^{\pm}$ decays to determine the acceptance for these μ's, Monte Carlo events are generated and in each event a $\pi^{\pm}$ or $K^{\pm}$ in a jet is selected and forced to undergo a two-body decay to $\mu\nu_{\mu}$. This decay is carried out in the rest frame of the π/K in random directions and then the 4-vector of the resulting μ is boosted and rotated into detector coordinates. The boost is determined by the $\pi^{\pm}$ or $K^{\pm}$ energy. The final step is calculating and assigning the appropriate decay probability for each $\pi^{\pm}$ and $K^{\pm}$.

In general for a particle with a measured lifetime τ, the probability that this particle remains after time t is:

$$exp\left(\frac{-t}{\tau}\right)$$

When the particle is relativistic, the apparent lifetime is $\tau \rightarrow \gamma\tau\prime$ where $\tau\prime$ is the lifetime of the particle at rest in the observer's frame. For a relativistic particle the time t it takes to travel a distance L is $t = \dfrac{L}{\beta c}$. The probability that this particle will remains after traversing a distance L is given by :

$$P = \exp\left(\frac{-L}{\beta\gamma c\tau}\right)$$

To estimate the decay probability of $\pi^{\pm}$'s and K's, L is taken to be the distance form the vertex to the edge of the calorimeter (L_{air}) plus one absorption length (λ_A) in the calorimeter. The quantity λ_A is the mean distance a π/K will travel before undergoing an inelastic collision with a nucleus. This distance is a function of the cross-section for π/K-nucleon scattering which is energy dependent. Its value is experimentally determined for a range of π/K energies so there is a systematic uncertainty associated with its value. For the purposes of this calculation it is assumed that after one absorption length the π/K will scatter out of consideration, and there is a further uncertainty associated with this assumption : It is possible that following the inelastic collision a π/K could be travelling more or less in the same direction as the original π/K and with similar energy.

The probability the π/K will not decay in L_{air} is:

$$\mathrm{P(air)} = \exp\left(\frac{-L_{air}}{\gamma\beta c\tau}\right)$$

And the probability that it does not decay within one λ_A is:

$$\mathrm{P(abs)} = \exp\left(\frac{-\lambda_A}{\gamma\beta c\tau}\right)$$

The probabillity that the the π/K remains after traversing $L_{air} + \lambda_A$ is then:

$$\mathrm{P(remains)} = \exp\left(\frac{-(L_{air} + \lambda_A)}{\gamma\beta c\tau}\right)$$

And thus the probability it decays in the same distance is:

$$\mathrm{P(decays)} = 1 - \mathrm{P(remains)}$$

The total distance L depends on the vertex position and the trajectory angle of the π/K with respect to the beam line.

As an example, a randomly selected jet (generated by Monte Carlo) had $E_T =$ 32.1GeV and was at $\eta_{jet} = 0.05$. There were 3 $\pi^{\pm}$'s with energies $5.3, 6.6$ and 8.6GeV (there were no $K^{\pm}$ in this event and charged hadrons with energy $<$ 4GeV are not considered). At $\eta = 0$ the distance through air to the edge of the calorimeter is 0.7 m and 1 λ_A in the calorimeter corresponds to 0.32 m. The probability that this jet will contain a $\mu^{\pm}$ from a $\pi^{\pm}$ decay is taken to be the sum of probabilities for each $\pi^{\pm}$ to decay, in this case PDK $= 0.0034+0.0028+0.0021 =$ 0.0083 or there's a probability of 1% that this jet will have a μ of at least 4GeV/c momentum from a $\pi^{\pm}$ decay.

There is a systematic uncertainty in calculating the probability of a $\pi^{\pm}$ (and hence $K^{\pm}$) decay. The value of λ_A is determined experimentally and depends on the $\pi^{\pm}$/nucleon cross-section (which is energy dependent).

To consider the total probability that a given $\pi^{\pm}$ decays After obtaining the decay μ, a search is made for the nearest PJET. PJETs are particle level jets determined using an algorithm similar to the one described in the data section for jet reconstruction but using the final state particles in the generated event instead of calorimeter towers.

When the nearest PJET is found the PJET energy is smeared according to the calorimeter resolution and the muon momentum is smeared according to the

muon momentum resolution. For muons which pass the applicable acceptance requirements the P_T^{rel} and $Z_{\|}$ are calculated. The muon acceptance requirements are that the muon has at least 4 GeV/c momentum, has $|\eta_\mu| < 1.0$ and is within ΔR of 0.5 of the jet. The jet is required to have $|\eta| < 0.6$ and $E_T^{jet} > 10$ GeV. If the muon parent π or K is found within the PJET cone, the π or K momentum is vectorially removed from the PJET before the jet energy is smeared.

The estimated relative number of muons in jets from $\pi^{\pm}/K^{\pm}$ decays with respect to the total number of muons from all Monte Carlo sources, by E_T^{jet} bins and for the total data set, are listed in table 7.

The plots in Fig. 22 show the resulting distributions of P_T^{rel} and $Z_{\|}$ used in evaluating the fit.

6.2.2 Heavy Quark Estimates

To generate the characteristic distributions for b and c decays to muons, unbiased events are generated and events are selected which contain final state muons from weak decays of b and c mesons. The muons are required to be associated with PJETS in those events. The quark source (whether the quark is directly produced or the result of gluon splitting) is determined and the P_T^{rel} and $Z_{\|}$ are calculated. Calorimeter and muon smearing are done on both the PJET and muon (as was done with the $\pi/K\mu$ sample).

To reflect the effect of jet triggering on the data set, a weighting based on the distribution of jet E_T in the data set is imposed. This has the effect of giving the same distribution of E_T^{jet} in the Monte Carlo events as that found in the data set. This is important because the momentum fraction distribution for muons

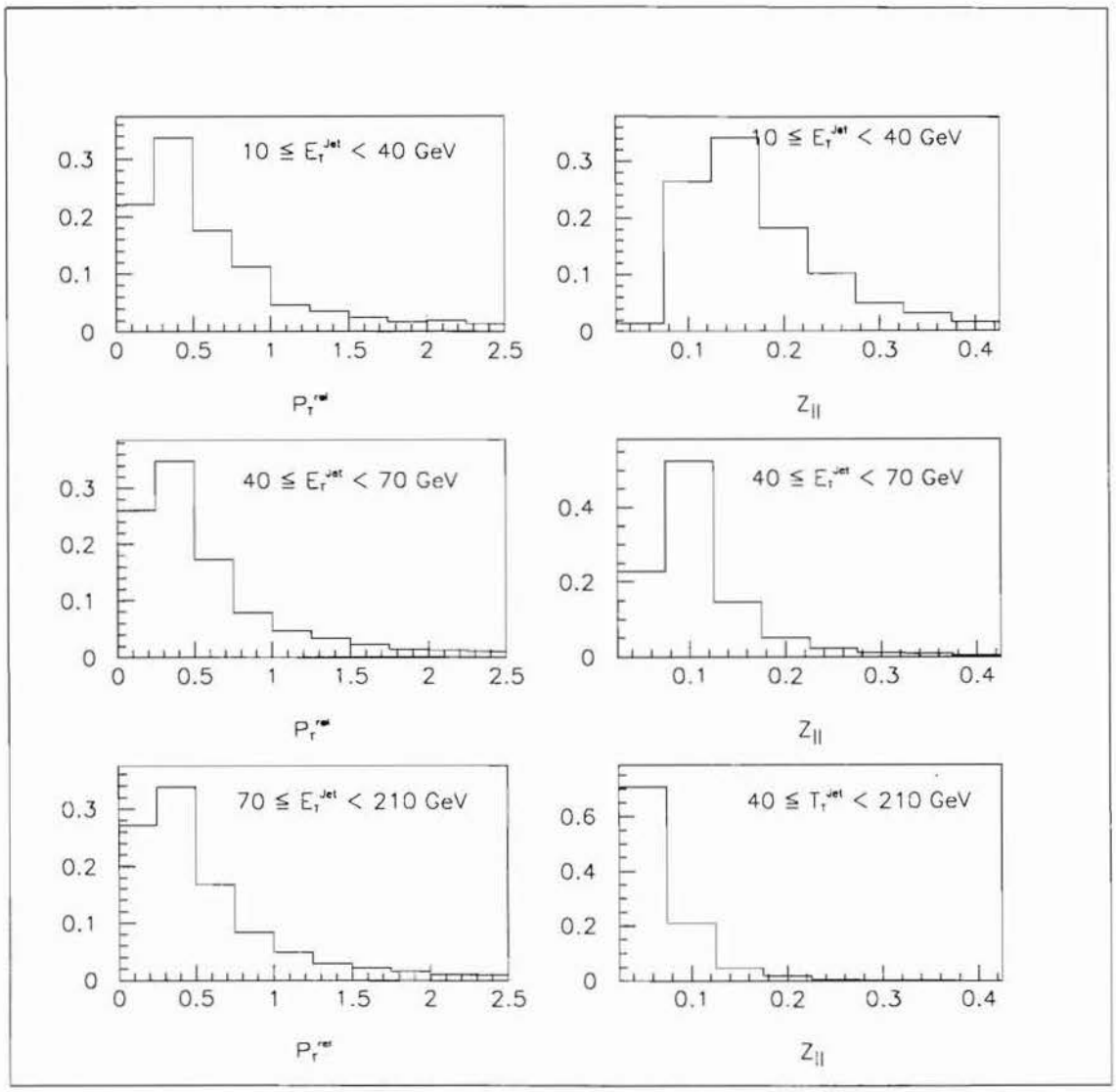

Figure 22: HERWIG generated $\pi/K \rightarrow \mu$ distributions

Table 7: MC Estimates for Relative abundances of muons from different sources in jets

Muon Source	10 - 40 GeV	40 - 70 GeV	70 - 210 GeV	Total E_T range
$\pi^{\pm}/K^{\pm}$	25.86%	15.53%	10.12%	17.12%
c	10.41%	12.55%	14.09%	11.80%
b	4.68%	4.98%	4.56%	4.54%
$g \rightarrow c\bar{c}$	34.59%	43.80%	54.00%	42.78%
$g \rightarrow b\bar{b}$	24.46%	23.16%	17.23%	23.76%

from quarks from gluon splitting will be very dependent on the E_T^{jet}. There is also some effect on the P_T^{rel} distributions but not to as great a degree.

The characteristic distributions for muons in jets from c and b are shown in figs 23 and 24. In each plot the corresponding characteristic function for μ's from π/K decays is superimposed. All plots have been normalized to unity. The (Monte Carlo) estimated percentages of muons in jets for each source ($\pi, K, c, b, g \rightarrow c\bar{c}, g \rightarrow b\bar{b}$) for the total data set and for each jet E_T bin is given in table 7.

6.2.3 Jet Widths

One way to distinguish gluon jets containing heavy quarks from heavy quark jets is by the width of the jet in the calorimeter. The rms η width and rms ϕ widths for jets from the data are determined according to:

$$w_{\eta}^{rms} = \frac{1}{E_{T,tot}} \sqrt{\sum_i (E_{Ti} \times \Delta\eta)^2}$$

and

$$w_{\phi}^{rms} = \frac{1}{E_{T,tot}} \sqrt{\sum_i (E_{Ti} \times \Delta\phi)^2}$$

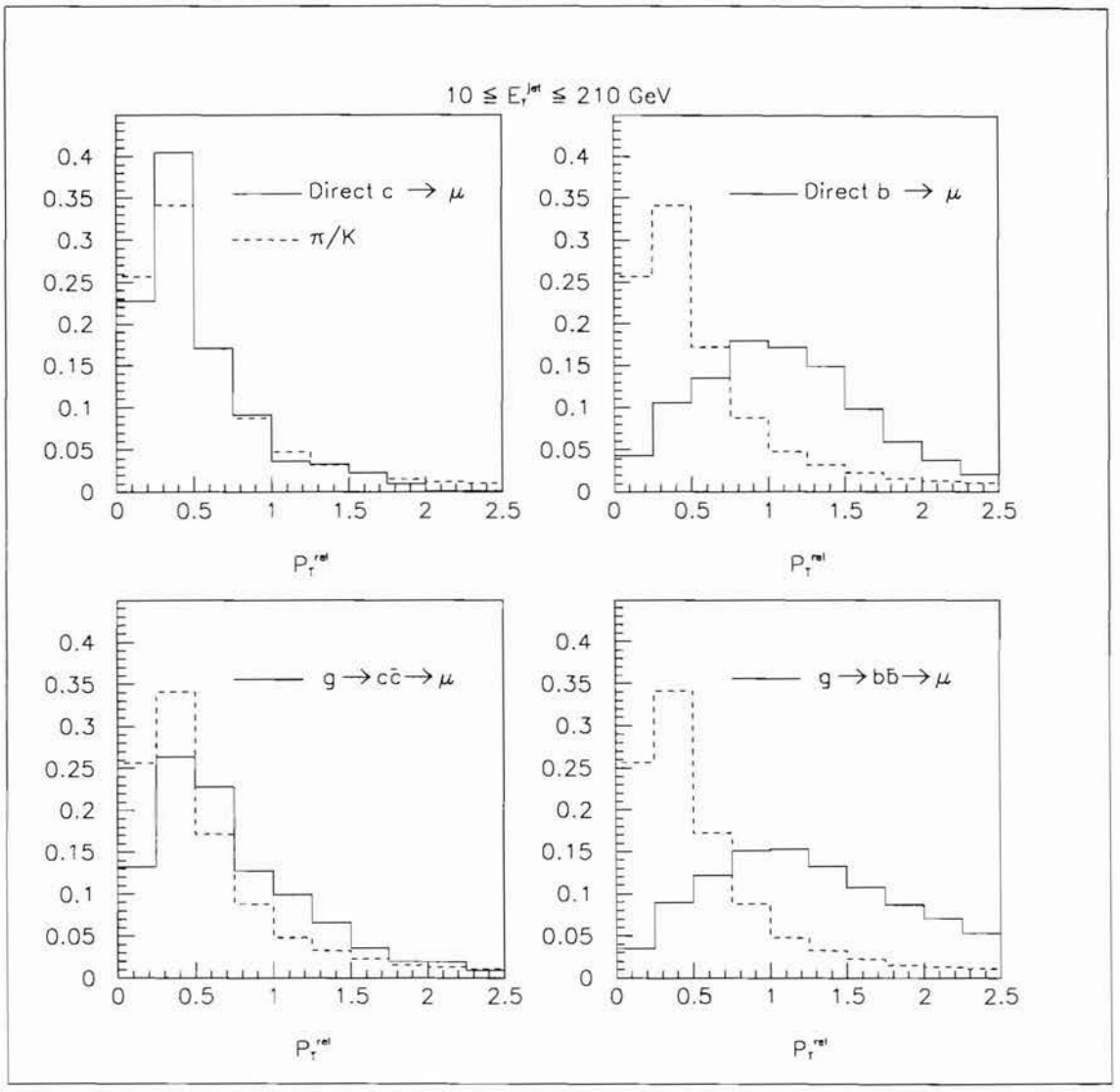

Figure 23: HERWIG generated $b/c \rightarrow \mu$ distributions

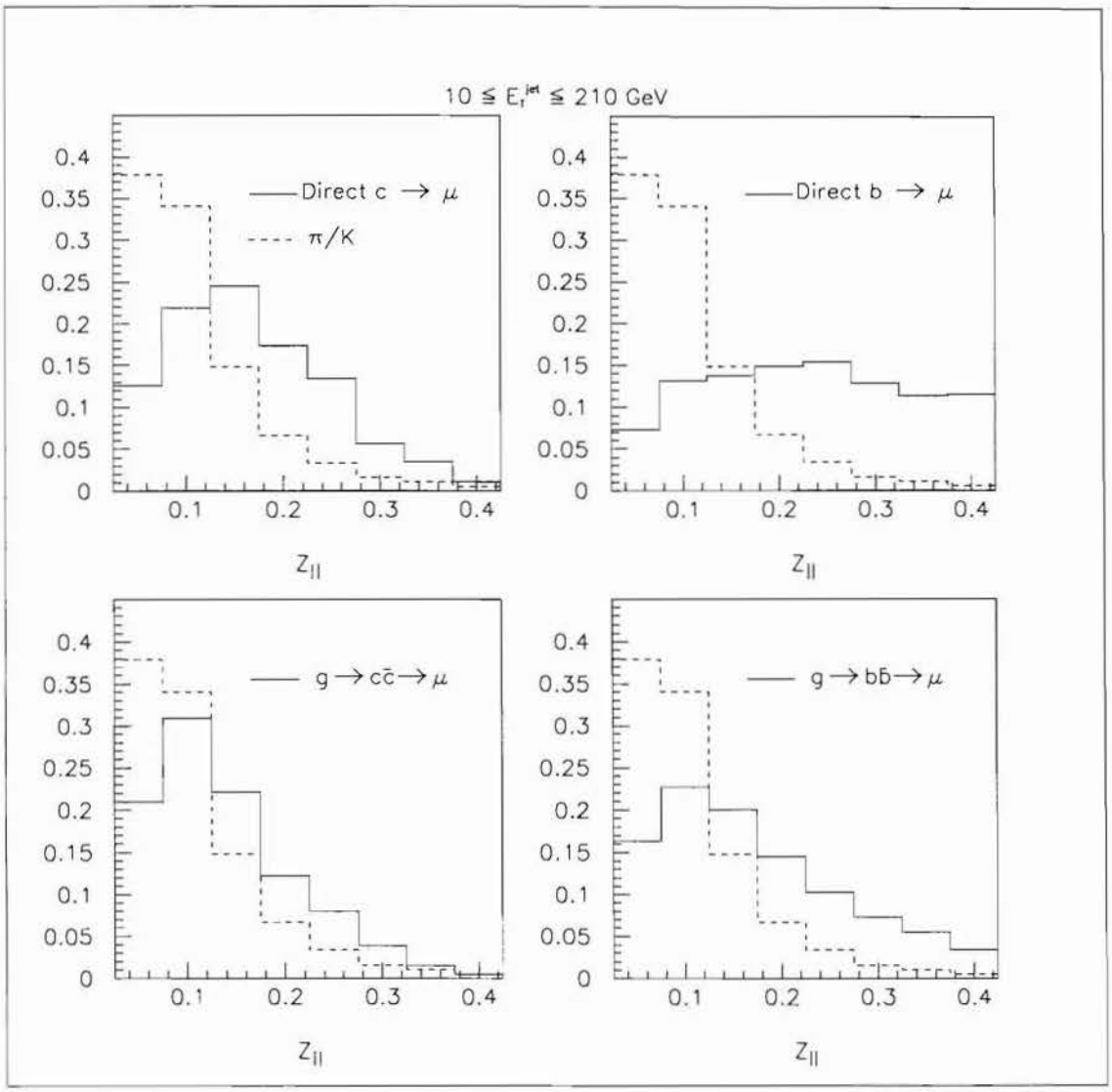

Figure 24: HERWIG generated $b/c \rightarrow \mu$ distributions

In each case the sum is over calorimeter towers and the Δ's are between the ith cell and the centroid of the jet.

At the Monte Carlo generator level a similar calculation using final state particles can be performed and the results are shown in Fig. 25. The widths are determined for combined b and c quark jets and gluon jets containing $g \rightarrow c\bar{c}$ and $g \rightarrow b\bar{b}$.

A complete analysis would require full detector simulation of hadronic cascade effects on jet broadening before performing a fit to the data. At the particle level, differences in the widths of gluon and heavy quark jets appear which suggest that this is another tool for differentiating heavy quark and gluon jets containing heavy quarks, particularly when these jets have associated μ's because μ's can indicate the presence of heavy quarks.

6.2.4 Event Topologies

Another study performed at the generator level was on the frequency that a gluon jet (defined as a PJET with the closest parton to this jet being a gluon), which split into a $c\bar{c}$ or $b\bar{b}$ pair, contained one or both heavy quarks. This (quick and incomplete) study showed that over the E_T^{jet} range of the data set, for $c\bar{c}$, 33% had one quark contained by the PJET and 67% had both quarks contained by the PJET. For $b\bar{b}$, 56% had one quark contained by the PJET and 44% had both quarks contained by the PJET.

Full detector simulation and reconstruction would be needed to determine if, in the events where one quark was not associated with the parent parton (gluon) PJET, the quark was resolved as another jet. In this case there would be three

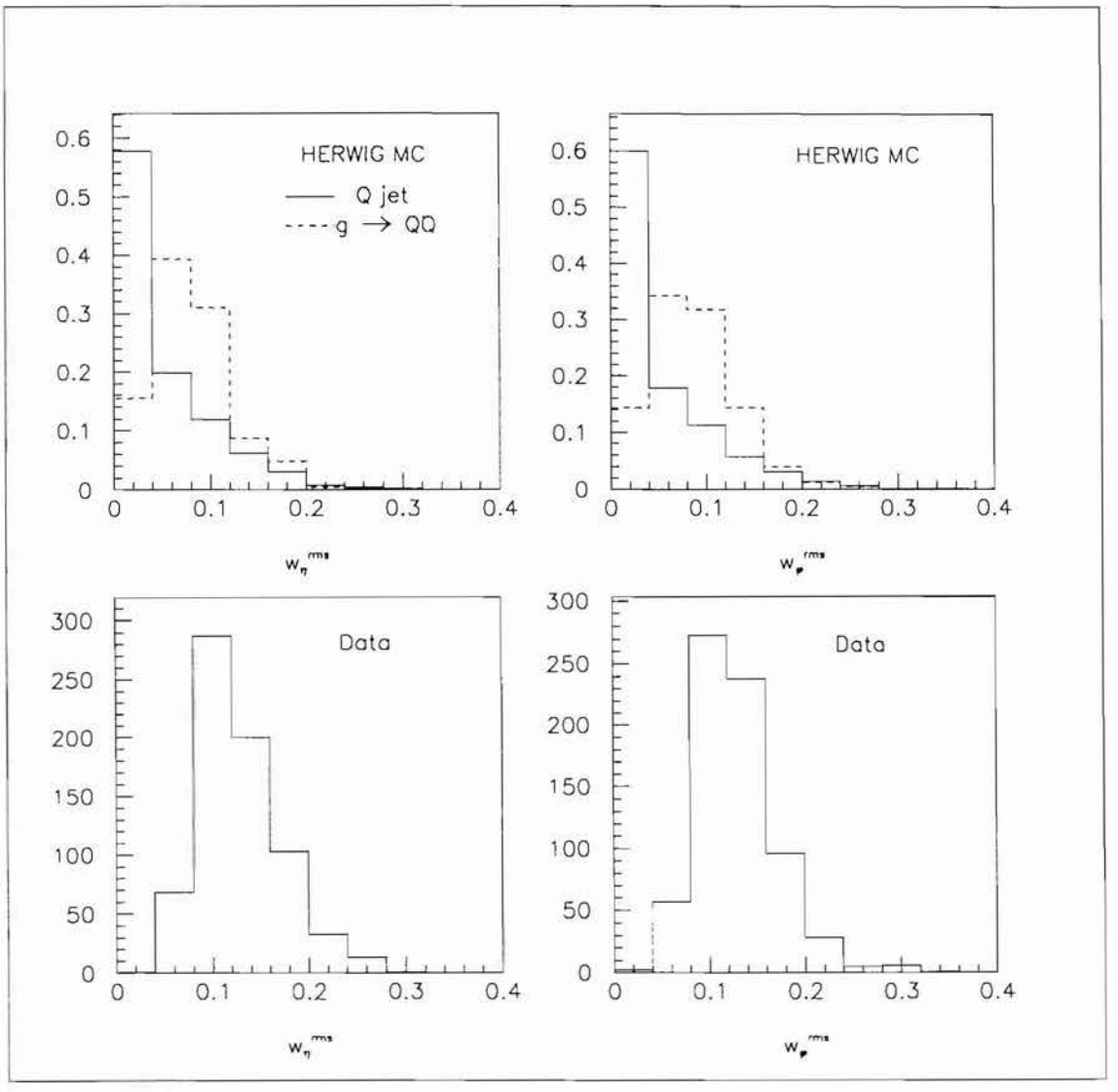

Figure 25: MC particle level compared with data RMS η and ϕ widths

Table 8: Estimated number of gluon jets by jet E_T bins

Jet E_T bin	$< n_{gluons} >$
10 - 40 GeV	$16729 \pm 48(syst) \pm 129(stat)$
40 - 70 GeV	$10867 \pm 20(syst) \pm 104(stat)$
70 - 210 GeV	$9217 \pm 4(syst) \pm 96(stat)$

jets. This study used PJETs resolved in $\Delta R < 0.5$ cones.

6.2.5 Gluon Jet Population Estimate

To estimate the abundance of gluon jets in each jet E_T bin, Monte Carlo events were generated using two different structure functions. Different structure function sets were used to estimate systematic errors for the abundances. The number of gluon jets in each sample was calculated by taking the ratio of gluon jets to total number of jets in 5 GeV bins, multiplying this number by the number of inclusive jets from the data set and summing 5 GeV bin totals for total numbers in the the three E_T^{jet} bins ($10 - 40$ GeV, $40 - 70$ GeV and $70 - 210$ GeV).

The structure function sets used are from PDFLIB [35] and are the MRS set H and CTEQ set 2P. The estimated rates from the two sets are shown together with the total jet E_T spectrum from the data set in Fig. 26.

6.2.6 Fits

The Monte Carlo two dimensional distributions used to fit the data are in bins of P_T^{rel} vs $Z_{\|}$.

A fit is made to the entire data sample (spanning the full range in E_T^{jet} with the results shown in Tables 9 and 10. Table 9 lists the contributions to the total

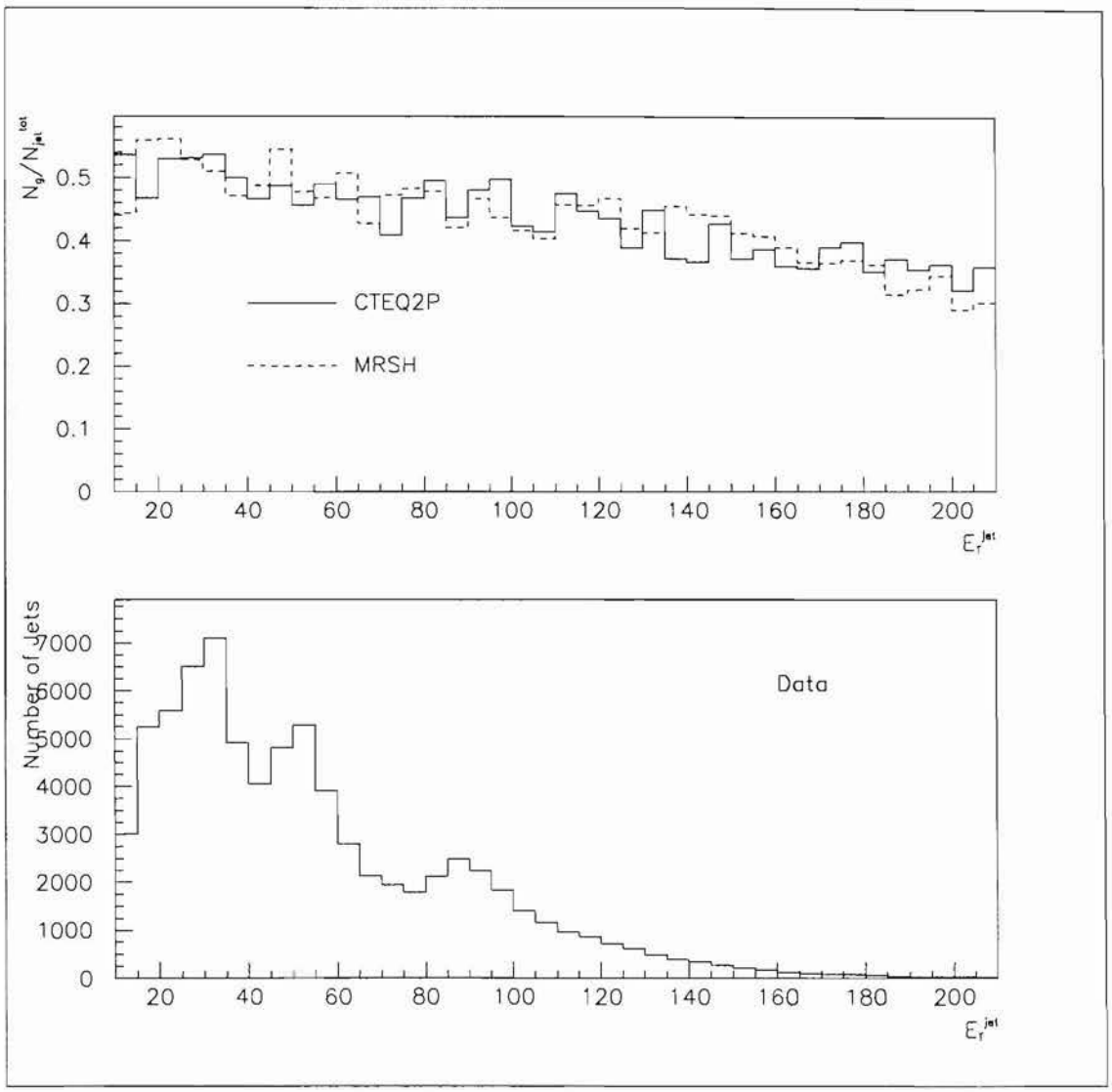

Figure 26: Distributions used to calculate the Number of Gluon Jets

number of muons by source in an unconstrained fit. Also shown in Table 9 are the Monte Carlo calculated abundances of each source. In Table 10 μ's from different sources (excluding muons from b/c from gluon splitting) are constrained to their respective Monte Carlo abundances, separately and in combination. Both tables list the Confidence Levels for the fits.

Fits are made to subsets in bins E_T^{jet} so that a comparison can be made with the analytic estimates of Mangano and Nason. The number of μ's in each E_T^{jet} bin from constrained fits (the abundances of μ's from π/K decays,from direct b and direct c are constrained to the Monte Carlo calculated abundances) are listed in Table 11. The Confidence Level for the fit in the third bin (0.26%) is poor because of the poorness of fit in $Z_{\|}$ dimension. Projections from the two-D fit are shown in Fig. 29.

The fits are performed by MINUIT [36] and are made by minimizing the log of the liklihood function :

$$L = \prod_{i=1}^{nevent} \sum_{j=1}^{nprocess} N_j \prod_{k=1}^{nvar} f_{jk}(x_{ik})$$

where the variables f_{jk}, P_T^{rel} and $Z_{\|}$, are related because they're both dependent on muon momentum. The N_j's are fit for the abundances.

Fig. 27 shows the fit contour for the $g \rightarrow c\bar{c}$ and $g \rightarrow b\bar{b}$ μ's in the completely unconstrained fit (Table 9). Fig. 28 shows the P_T^{rel} and $Z_{\|}$ projections in the total fit compared with the data set. From the number of muons in the fit the number of quark pairs is estimated to be:

$$N^{Q\overline{Q}} = n_{fit}^{\mu} \times \frac{1}{\epsilon_{reco}^{\mu}} \times \frac{1}{2 \times Br(Q \rightarrow \mu)}$$

where n_{fit}^{μ} is obtained from table 11. A muon reco efficiency of 0.5 ± 0.03 was used.

Table 9: Unconstrained fit and Monte Carlo estimates for numbers of muons by source in total data set

$10 \leq E_T^{jet} < 210 GeV$		
μ Source	Uncon. Fit	MC Est.
π/K	147.92 ± 34.40	92.81
direct c	-8.23 ± 31.57	63.95
direct b	37.22 ± 23.31	24.61
$g \rightarrow c\bar{c}$	252.07 ± 59.16	231.88
$g \rightarrow b\bar{b}$	113.03 ± 37.39	128.75
C. L.	37.5%	34.1%

Table 10: Constrained fits for numbers of muons by source for the total data set

$10 \leq E_T^{jet} < 210 GeV$				
Source	π/K	π/K & c	π/K & b	π/K & c & b
π/K	92.81(fixed)	92.81(fixed)	92.81(fixed)	92.81(fixed)
direct c	-4.74 ± 31.88	63.95 (fixed)	-0.88 ± 30.31	63.95
direct b	33.08 ± 22.39	18.90 ± 20.92	24.61 (fixed)	24.61
$g \rightarrow c\bar{c}$	305.50 ± 49.76	223.06 ± 30.41	299.49 ± 47.29	224.24 ± 30.15
$g \rightarrow b\bar{b}$	110.63 ± 36.65	142.92 ± 35.00	120.93 ± 25.48	136.44 ± 25.45
C. L.	29.5%	26.9%	30.0%	31.3%

Table 11: Constrained fits for numbers of muons by E_T^{jet} bins

Source	$10 \leq E_T^{jet} \leq 40\ GeV$	$40 \leq E_T^{jet} \leq 70\ GeV$	$70 \leq E_T^{jet} \leq 210\ GeV$
π/K	40.08 (fixed)	29.20 (fixed)	19.63 (fixed)
direct c	16.14 (fixed)	23.59 (fixed)	27.33 (fixed)
direct b	7.25 (fixed)	9.36 (fixed)	8.85 (fixed)
$g \rightarrow c\bar{c}$	28.48 ± 11.63	80.62 ± 15.26	81.94 ± 22.82
$g \rightarrow b\bar{b}$	63.13 ± 11.85	38.38 ± 12.12	58.36 ± 20.42
C. L.	70.4%	26.9%	0.26%

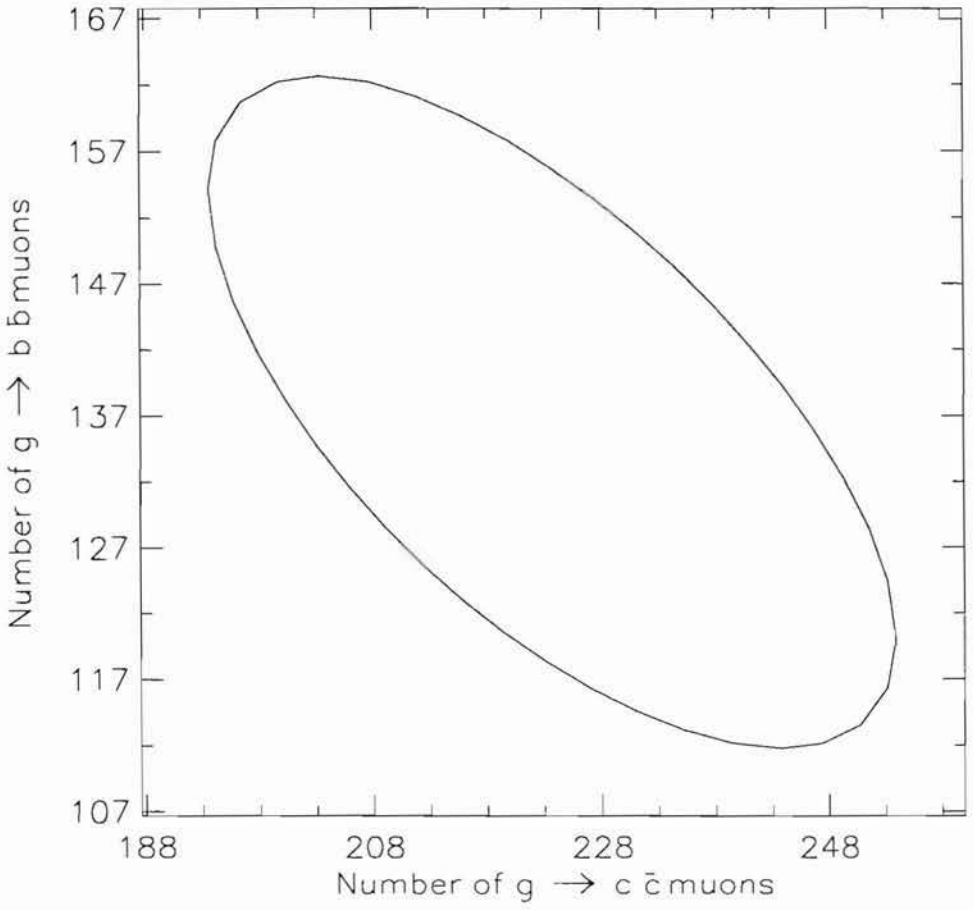

Figure 27: Fit contour for $g \to c\bar{c}$ vs $g \to b\bar{b}$

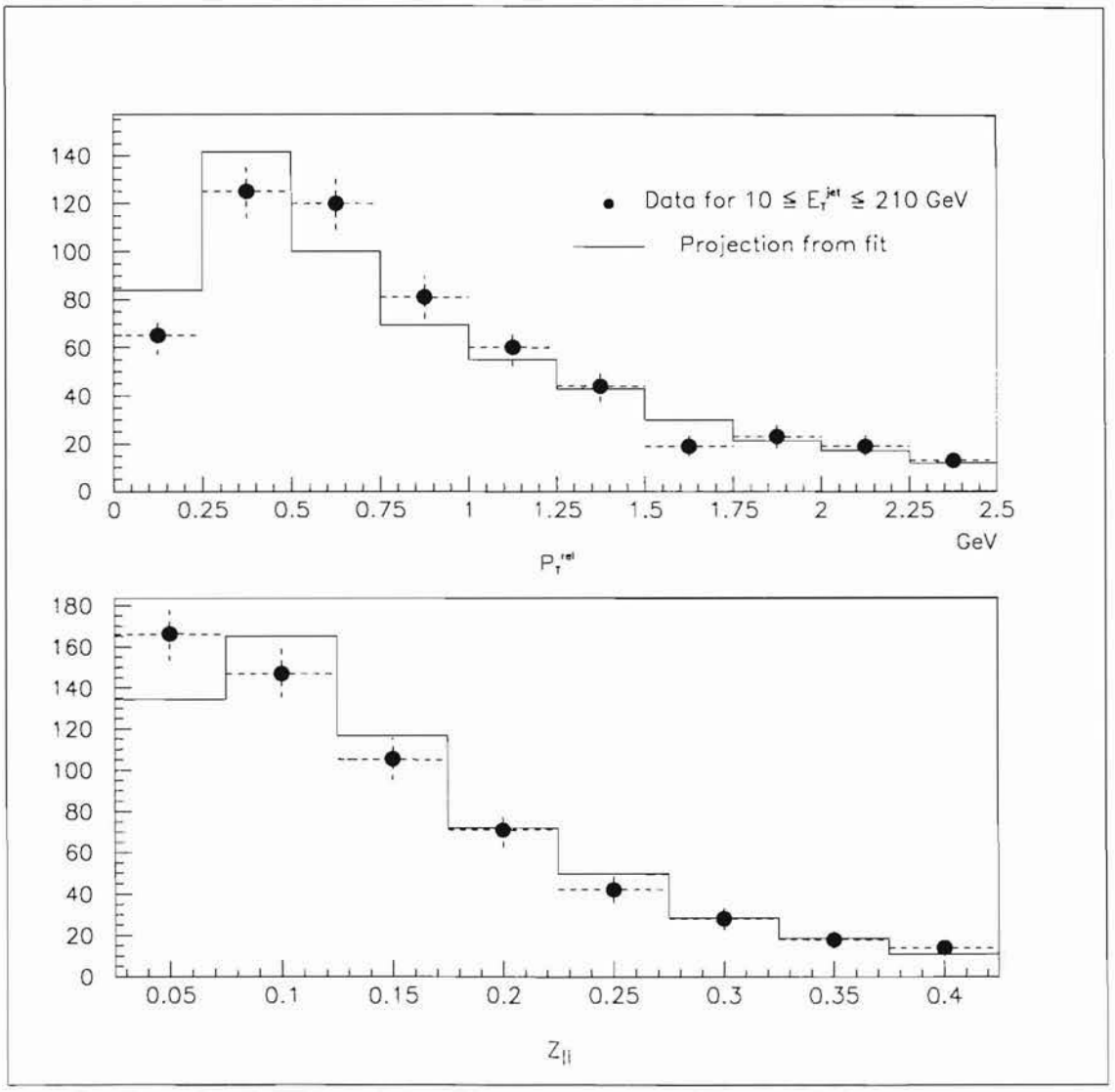

Figure 28: Projections for fit to total data set by sources

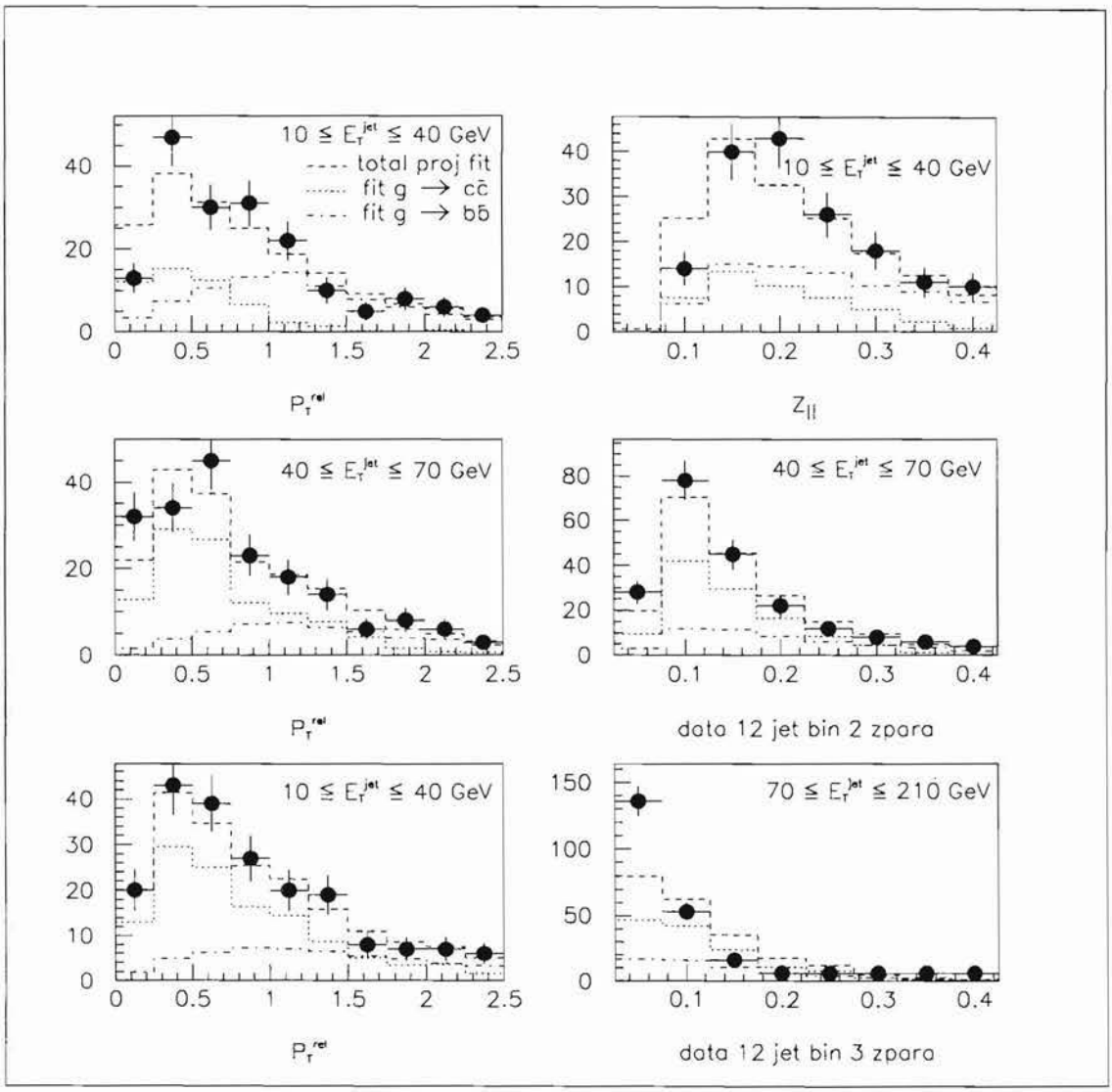

Figure 29: Projections of fit results compared to data in jet E_T bins

This value was determined from Monte Carlo studies using full detector simulation (DØ Geant) and muon reconstruction ([16]). The branching ratio used for $c \rightarrow \mu$ was 12.99 $^{+3.15}_{-2.78}$ % and for b $10.3 \pm 0.5\%$. The systematic uncertainty in amount π/K μ's is taken to be 15% (absolute) [16] while the systematic uncertainty for Monte Carlo generation of direct c and b, and hence for the muons from these sources, is taken to be 5%.

The systematic error attributed to Monte Carlo uncertainty in the abundance of μ's from π/K decays, direct c and direct b decays is taken all together. It is calculated as the maximum change in the fit number of μ's by source ($g \rightarrow c\bar{c}$ and $g \rightarrow b\bar{b}$) in each E_T^{jet} bin, when the amount of π/K, c and b μ's are constrained to within their respective systematic uncertainties.

Tables 12 and 13 give the mean rates for the binned fits for $g \rightarrow c\bar{c}$ and $g \rightarrow b\bar{b}$ and list the various statistical and systematic errors. Total systematic errors are the result of summing the individual systematic errors and the same for the total statistical errors. The results for the calculated rates for quark pairs in gluon jets with errors are given in table 14. Plots in Figs 30, 31, 32, 33, 34, 35 show the calculated rates for quark pairs from this analysis. They are compared with analytic estimates from Mangano and Nason for c quark mass 1.5 GeV and for different b quark masses. Also shown on the c plot is a point obtained from CDF which measured the rate of D production in an inclusive jet sample.

While the fit points for $g \rightarrow c\bar{c}$ are generally lower than theoretical estimates, they are consistent. There are larger systematic errors than statistical errors with the $g \rightarrow c\bar{c}$ fits while for the $g \rightarrow b\bar{b}$ the opposite is true. This was also shown in the correlation between characteristic shapes for the π/K and c and $g \rightarrow c\bar{c}$ μ

Table 12: Errors for rate for g$\rightarrow c\bar{c}$

Jet E_T range	10 - 40 GeV	40 - 70 GeV	70 - 210 GeV
Fit mean rate	0.0131	0.0571	0.0684
fit $\pi/K/c/b$	$^{+0.0032}_{-0.0024}$	$^{+0.0055}_{-0.0052}$	$^{+0.0082}_{-0.0082}$
BR(c$\rightarrow \mu$)	$^{+0.0036}_{-0.0026}$	$^{+0.0156}_{-0.0111}$	$^{+0.0187}_{-0.0133}$
$\epsilon_R(\mu)$	$^{+0.0008}_{-0.0007}$	$^{+0.0037}_{-0.0032}$	$^{+0.0044}_{-0.0038}$
$< n_{gluons} >$	< 0.0001	< 0.0001	< 0.0001
Total Syst.	$^{+0.0076}_{-0.0057}$	$^{+0.0248}_{-0.0195}$	$^{+0.0313}_{-0.0253}$
Stat fit	± 0.0054	± 0.0108	± 0.0191
Stat n_{gluons}	± 0.0001	± 0.0006	± 0.0008
Total Stat.	± 0.0054	± 0.0108	± 0.0191

Table 13: Errors for rate for g$\rightarrow b\bar{b}$

Jet E_T range	10 - 40 GeV	40 - 70 GeV	70 - 210 GeV
Fit mean rate	0.0366	0.0343	0.0615
fit $\pi/K/c/b$	$^{+0.0008}_{-0.0005}$	$^{+0.0009}_{-0.0008}$	$^{+0.0022}_{-0.0027}$
BR(c$\rightarrow \mu$)	$^{+0.0019}_{-0.0017}$	$^{+0.0017}_{-0.0016}$	$^{+0.0031}_{-0.0029}$
$\epsilon_R(\mu)$	$^{+0.0024}_{-0.0020}$	$^{+0.0022}_{-0.0019}$	$^{+0.0039}_{-0.0035}$
$< n_{gluons} >$	< 0.0001	< 0.0001	< 0.0001
Total Syst.	$^{+0.0051}_{-0.0042}$	$^{+0.0048}_{-0.0043}$	$^{+0.0092}_{-0.0091}$
Stat fit	± 0.0069	± 0.0108	± 0.0215
Stat n_{gluons}	± 0.0003	± 0.0003	± 0.0007
Total Stat.	± 0.0069	± 0.0108	± 0.0215

Table 14: Rates and errors by E_T^{jet} bin

Bin	$dN^{Q\bar{Q}}/dN_{gluonjets} for g \rightarrow c\bar{c}$	$dN^{Q\bar{Q}}/dN_{gluonjets} for g \rightarrow b\bar{b}$
1	$0.0131 \begin{smallmatrix}+0.0076\\-0.0057\end{smallmatrix} (syst) \pm 0.0054(stat)$	$0.0366 \begin{smallmatrix}+0.0051\\-0.0042\end{smallmatrix} (syst) \pm 0.0069(stat)$
2	$0.0571 \begin{smallmatrix}+0.0248\\-0.0195\end{smallmatrix} (syst) \pm 0.0108(stat)$	$0.0343 \begin{smallmatrix}+0.0048\\-0.0043\end{smallmatrix} (syst) \pm 0.0108(stat)$
3	$0.0684 \begin{smallmatrix}+0.0313\\-0.0253\end{smallmatrix} (syst) \pm 0.0191(stat)$	$0.0615 \begin{smallmatrix}+0.0092\\-0.0091\end{smallmatrix} (syst) \pm 0.0215(stat)$

sources. The $g \rightarrow b\bar{b}$ points also are consistent with theoretical estimates.

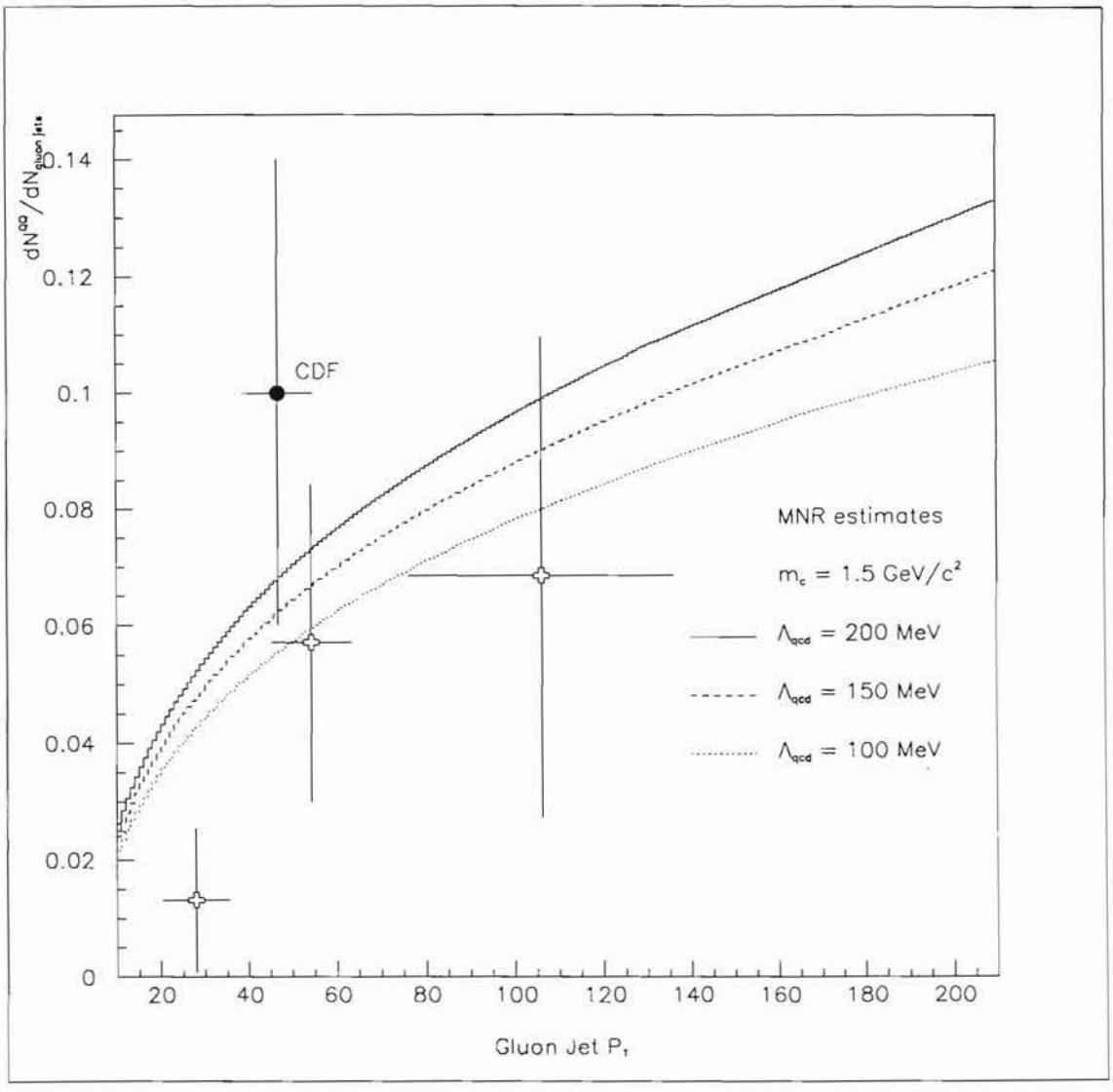

Figure 30: Rate for gluon splitting to $c\bar{c}$

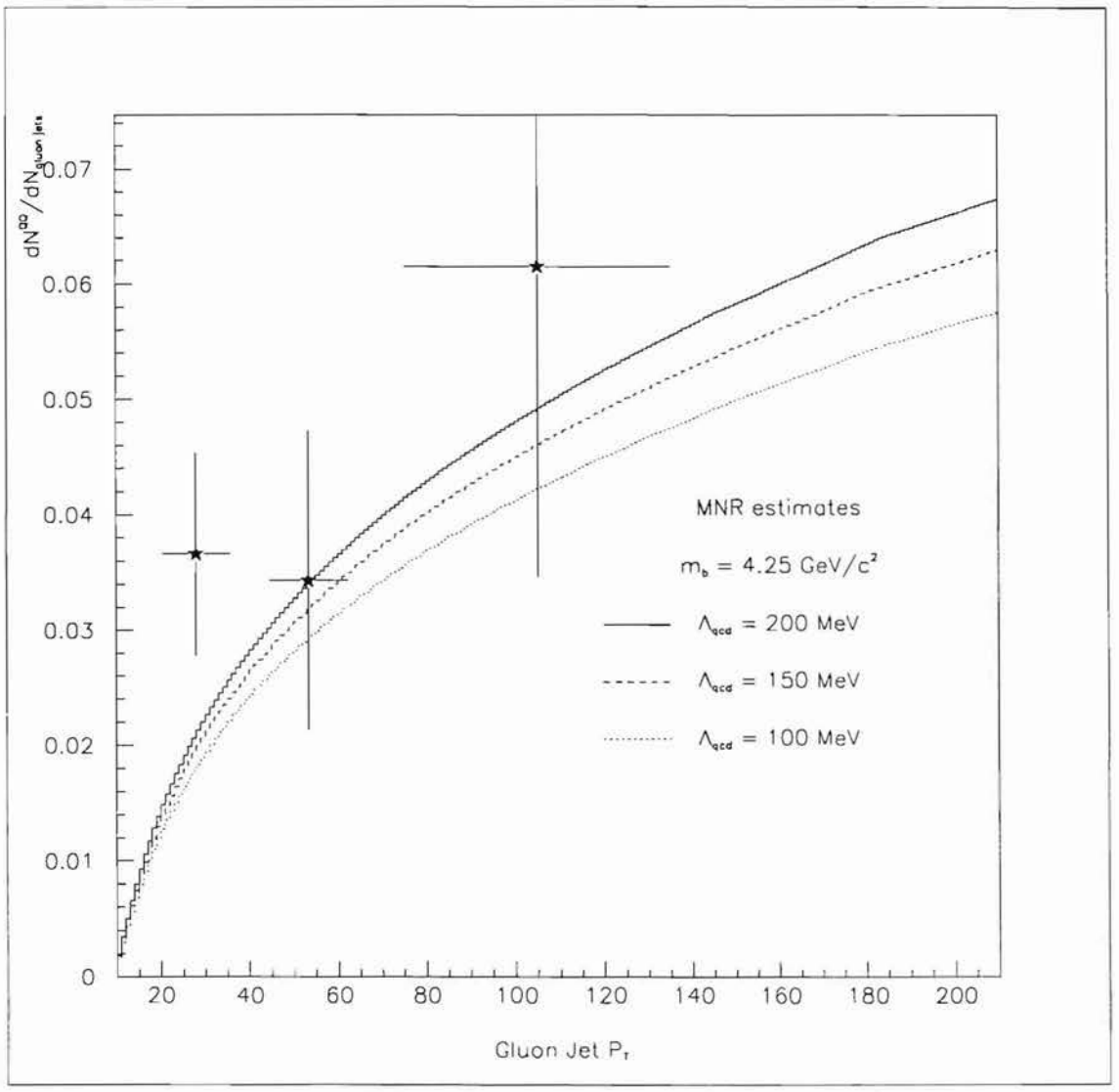

Figure 31: Fit for $g \rightarrow b\bar{b}$ and Estimate using $m_b = 4.25$ GeV/c^2

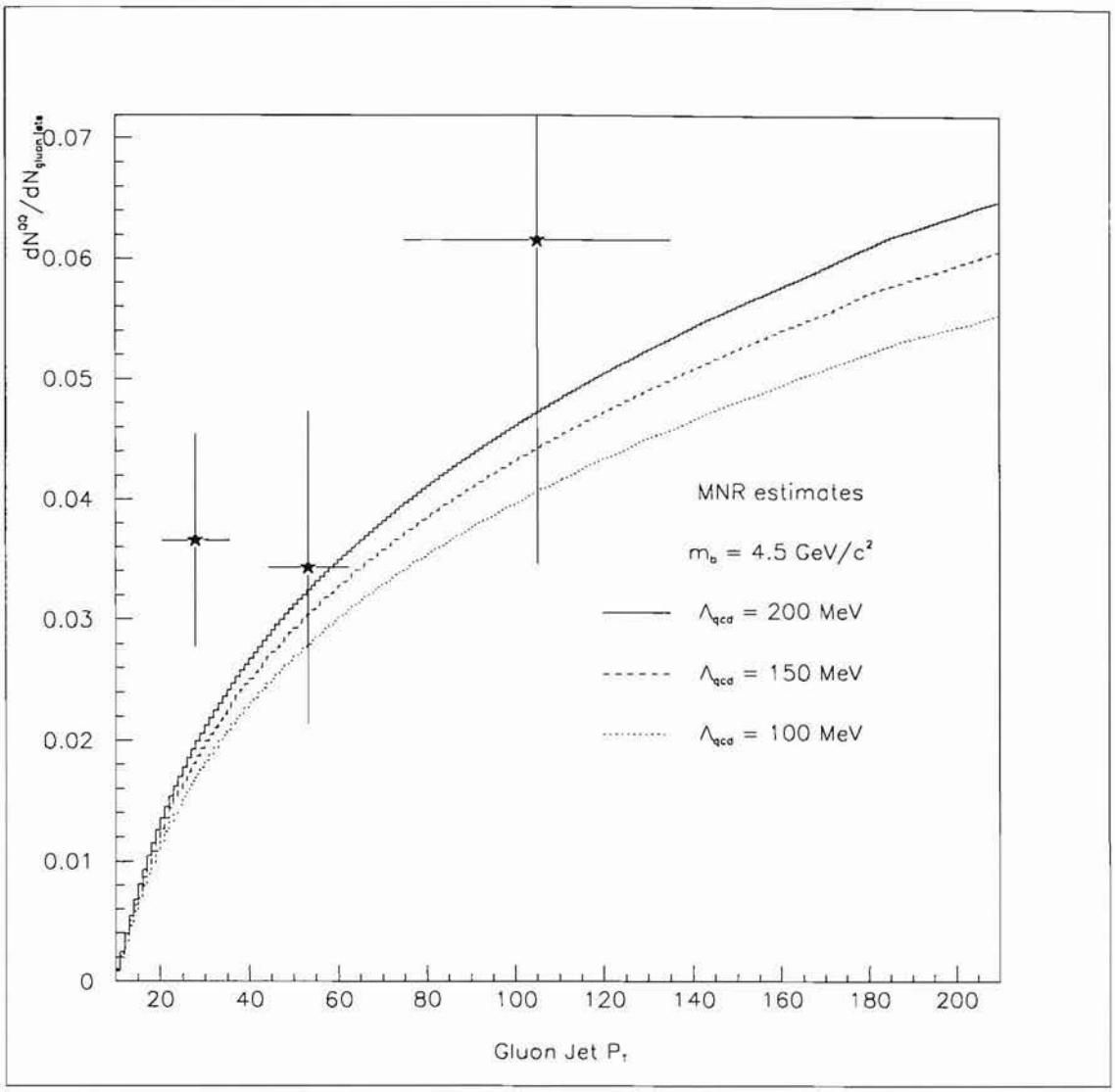

Figure 32: Fit for $g \rightarrow b\bar{b}$ and Estimate using $m_b = 4.5$ GeV/c^2

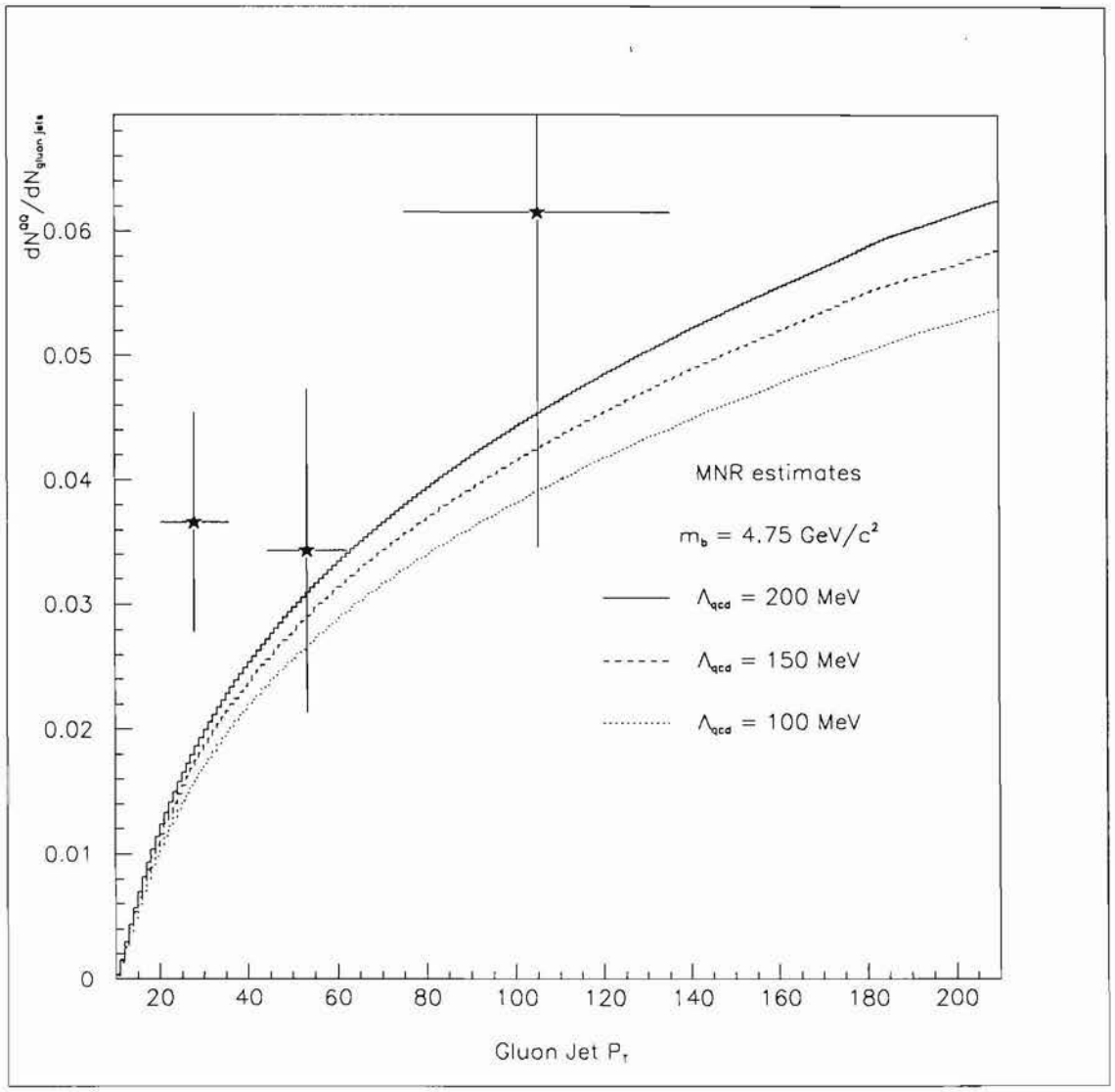

Figure 33: Fit for $g \rightarrow b\bar{b}$ and Estimate using $m_b = 4.75$ GeV/c^2

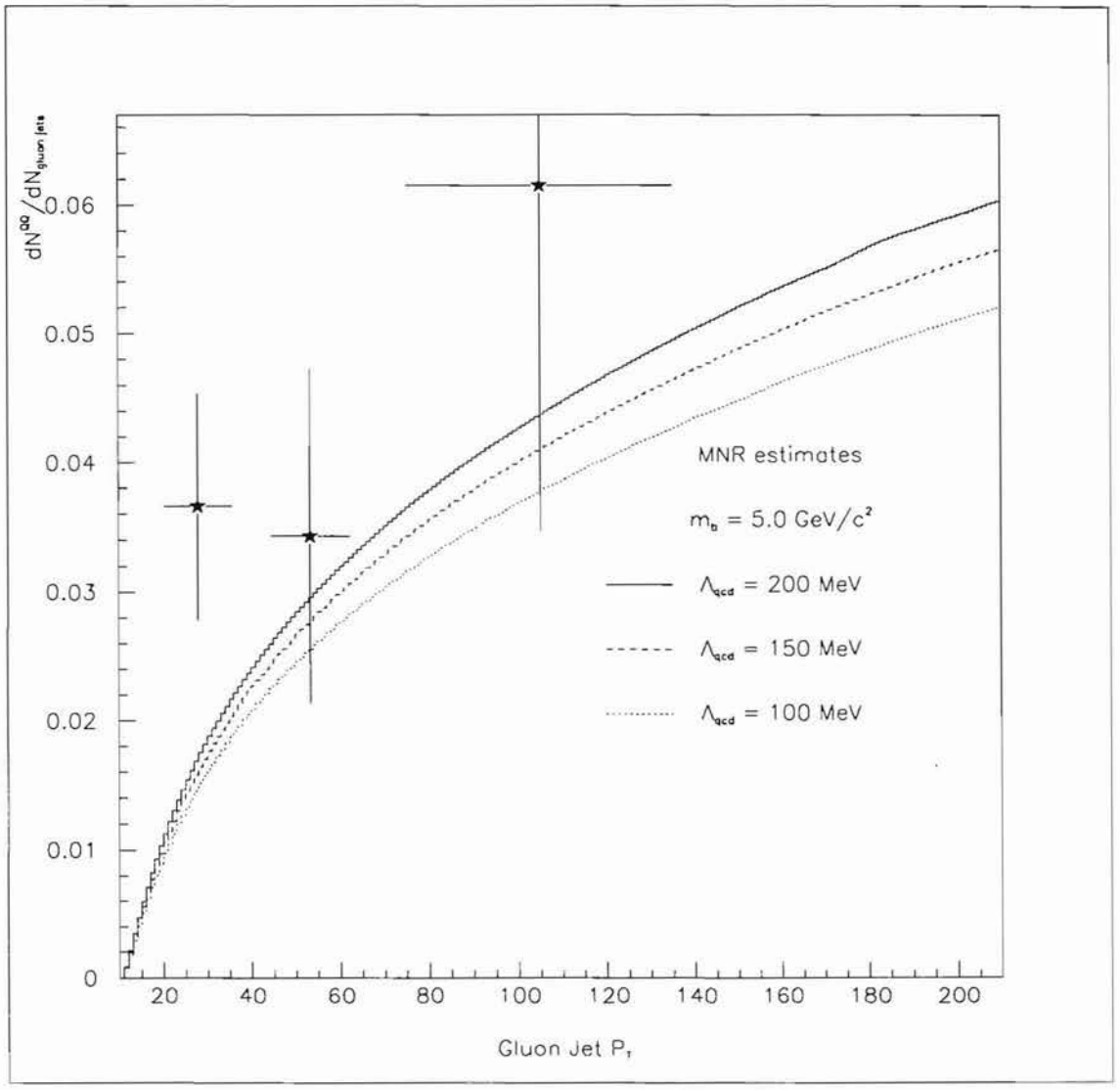

Figure 34: Fit for $g \rightarrow b\bar{b}$ and Estimate using $m_b = 5.0$ GeV/c^2

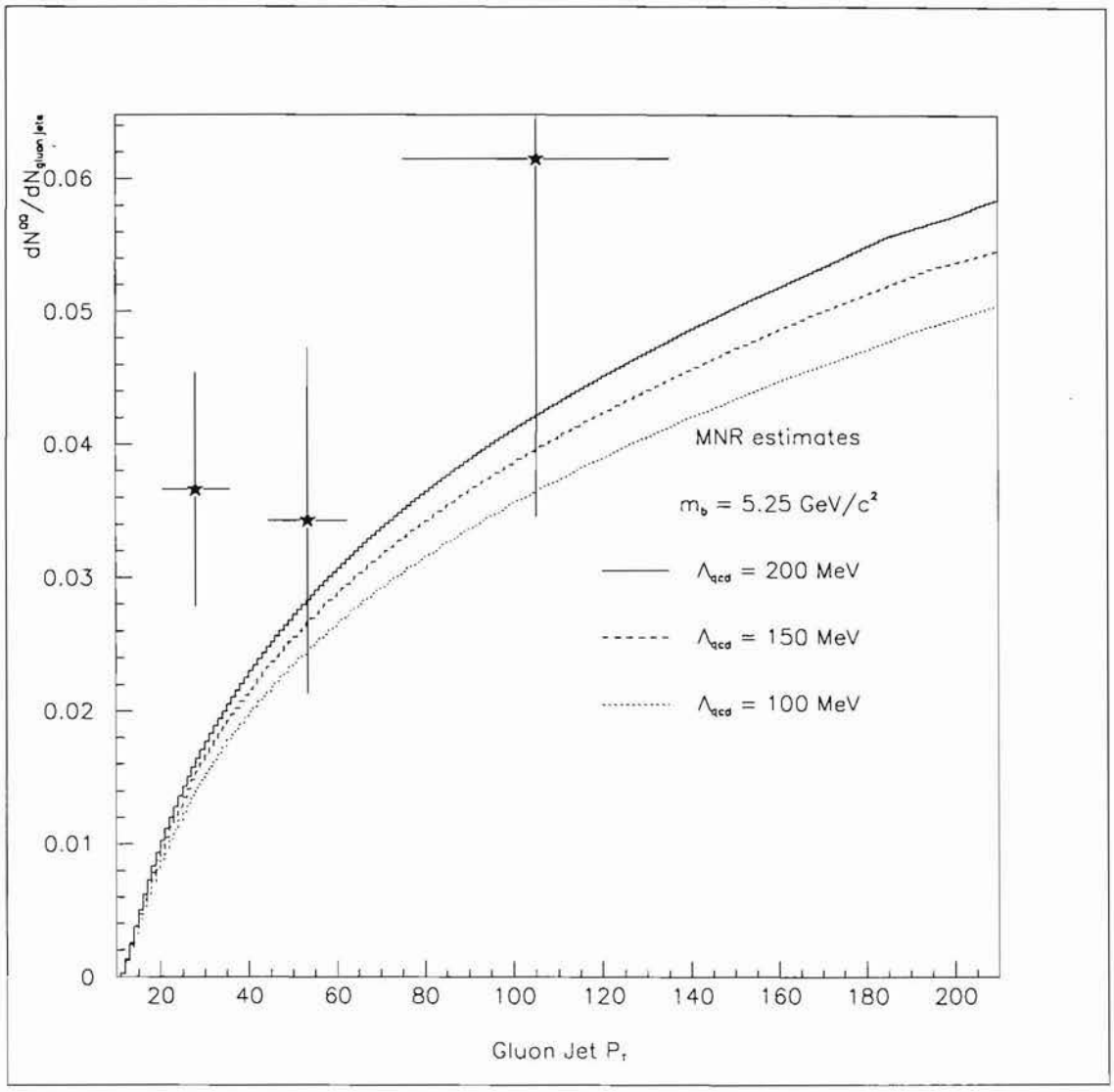

Figure 35: Fit for $g \rightarrow b\bar{b}$ and Estimate using $m_b = 5.25\mathrm{GeV/c^2}$

7 CONCLUSION

This analysis shows that muons in association with jets can be used to tag heavy quark sources of μ's (by P_T^{rel}) and indicate the source of those heavy quarks (either direct production or gluon splitting). Dimuon data sets would give cleaner signals for $Q\overline{Q}$ pairs and, at higher jet energies, would have smaller backgrounds from π/K decays.

This analysis supports perturbative QCD predictions for heavy quark production. In particular the results of this analysis are consistent with Next to Leading Order estimates by Mangano, Nason and Ridolfi for b quark production.

In the future, this analysis technique would be enhanced with the inclusion of a central magnetic field and precision vertex detector. With these upgrades in place, reconstructing decayed $B^{0,\pm}$ and $D^{0,\pm}$ from the charged light hadrons accompanying μ's would reduce the amount of mis-identification between c and b sources of μ's. In other words it would reduce the correlation between overall fits.

Also with an enhanced central detector, displaced vertices from $\pi^{\pm}/K^{\pm}$ decays would be detected and these sources of μ's could then be removed from the sample, reducing the background μ rate.

With a larger sample of low P_T μ's in association with lower energy jets ($E_T <$ 10 GeV), Monte Carlo predictions for the abundance of μ's from π/K decays could be tested to confirm Monte Carlo estimates for μ's from π/K decays in higher energy jets. This is because with lower energy jets there are relatively more decaying π/K's to decaying c and b quarks.

References

[1] S. Glashow, Nucl. Phys. 22 579 (1961);
S. Weinberg, Phys. Lett. ,12,132 (1967);
A. Salam,"Elementary Particle Physics", ed. N. Svartholm,367 (1968)

[2] J. Goldstone and S. Weinberg, Phys. Rev. 127,965 (1962);
P. W. Higgs, Phys. Lett. 12,132 (1964)
and Phys. Rev. Lett. 13 508 (1964)

[3] W. Marciano and H. Pagels, Phys. Rep. C,36,137 (1978)

[4] E. Abers and B. W. Lee, Phys. Rep. C, 9,1(1973);
C. N. Yang and R. L. Mills, Phys. Rev. 96 191 (1954)

[5] S. Glashow, J. Iliopoulos, L. Maiani, Phys. Rev. D, 2 (1970) 1285

[6] J. J. Aubert, et al. , Phys. Rev. Lett. 33 (1974) 1404;
J. E. Augustin, et al. , Phys. Rev. Lett. 33 (1974), 1406

[7] S. Herb et al. , Phys. Rev. Lett. , 39 (1977),252

[8] UA-1 Collab. , C. Albajar et al. , Phys. Lett. B256 (1991) 121;
UA-1 Collab. , C. Albajar et al. , CERN-PPE/93-153, Aug. 1993;
CDF Collab. , F. Abe et al. , FERMILAB-Conf-93/200-E (1993)

[9] N. Ellis and A. Kernan, Phys. Rep. 195 No. 2&3 Nov. 1990;
CDF Collab. , F. Abe et al. , Phys. Rev. Lett. 68 (1992) 3403;
CDF Collab. , F. Abe et al. , Phys. Rev. Lett. 69 (1992) 3704;

CDF Collab. , F. Abe et al. , Phys. Rev. Lett. 71(1993) 500;
CDF Collab. , F. Abe et al. , Phys. Rev. Lett. 71 (1993) 2396;
CDF Collab. , F. Abe et al. , Phys. Rev. D 50 (1994) 4252;
DØ Collab, S. Abachi et al. , Phys. Rev. Lett. 74 No. 18 1995) 3548

[10] G. Kopp,J. H. Kuhn and P. M. Zerwas, Phys. Lett. 153B No. 4,5(1985) p315

[11] M. L. Mangano, P. Nason and G. Ridolfi, Nucl. Phys. B 373 (1992) 295

[12] UA1 Collab. ,G. Arnison et al. ,Phys. Lett. 147B(1984) 222

[13] G.Kopp et al. ,Phys. Lett. 153B(1985) 315

[14] F. Halzen and G. Herzog, Phys. Rev. D30 (1984) 2326;
F. Halzen and P. Hoyer, Phys. Lett. B154 (1985) 324;
V. Barger and R. J. N. Phillips, Phys. Rev. D31 (1985) 215;
A. Ali and G. Ingelmann, Phys. Lett. B156 (1985) 111;
G. Kopp, J. H. Kuhn and P. Zerwas, Phys. Lett. B153 (1985) 315

[15] CDF Collab. ,F. Abe et al. ,Phys. Rev. Lett. 69 ,3704(1992);
CDF Collab. ,F. Abe et al. ,Phys. Rev. Lett. 71 ,500(1993);
CDF Collab. ,F. Abe et al. ,Phys. Rev. Lett. 71 ,2396(1993);
CDF Collab. ,F. Abe et al. ,Phys. Rev. D 50 ,4252(1994)

[16] S. Abachi et al. ,Phys. Rev. Lett. 74 , 3548 (1995)

[17] C. Peterson et al. ,Phys. Rev. D27(1) ,105(1983)

[18] L. M. Lederman, Sci. Am. Vol. 264 Num. 3 p52

[19] S. Abachi et al. ,Nucl. Instr. and Meth. , A388,185(1994)

[20] S. Abachi et al. ,Nucl. Instr. and Meth. , A324,53(1993)

[21] S. Aronson et al. ,Nucl. Instr. and Meth. ,A269,492(1988)

[22] S. J. Wimpenny et al. ,Nucl. Instr. and Meth. ,A279,107((1989)

[23] J. Yu, PhD. Thesis, SUNY at Stony Brook

[24] M. Mangano and P. Nason, Phys. Lett. B 285 (1992) 160-166

[25] C. Brown et al. ,Nucl. Instr. and Meth. ,A279,331(1989)

[26] James T. Linnemann, 'Triggering the D0 Experiment' D0 Note 1572

[27] J. Bantly et al. ,'The Level 0 Trigger for the D0 Detector' D0 Note 1996

[28] Jan Guida, 'The D0 Calorimeter Trigger' D0Note 1510

[29] G. Marchesini et al. ,Computer Physics Communications 67 (1992) 465

[30] E. S. Abers and B.W.Lee, Phys. Rep. 9C (1973) 1

[31] H. D. Politzer, Phys. Rep. 14C (1974) 129

[32] W. Marciano and H. Pagels, Phys. Rep. 36 C (1978) 137

[33] G. t'Hooft, Nucl. Phys. B33 (1971) 173;
G. t'Hooft, Phys. Lett. 37B (1971a) 195

[34] G. Marchesini and B. R. Webber, Nucl. Phys. B310 (1988) 461;
I. G. Knowles, Nucl. Phys. B310 (1988) 571;

S. Catani, G. Marchesini and B. R. Webber, Nucl. Phys. B349 (1991) 635;
G. Abbiendi and L. Stanco, Comp. Phys. Comm. 66 (1991) 16
and Zeit. Phys. C51 (1991) 81;
M. H. Seymour, Zeit. Phys. C56(1992) 161

[35] H. Plothow-Besch, 'PDFLIB: a library of all available parton density functions of the nucleon, the pion and the photon and the corresponding α_s calculations' Comp. Phys. Comm. 75 (1993) 396-416

[36] F. James and M. Roos, 'Minuit Users Guide' Program Library D506. CERN, 1981